

# 1 Gas-to-particle partitioning of major biogenic oxidation products: A 2 study on freshly formed and aged biogenic SOA

3 Georgios I. Gkatzelis<sup>1</sup>, Thorsten Hohaus<sup>1</sup>, Ralf Tillmann<sup>1</sup>, Iulia Gensch<sup>1</sup>, Markus Müller<sup>2,4</sup>,  
4 Philip Eichler<sup>2†</sup>, Kang-Ming Xu<sup>3</sup>, Patrick Schlag<sup>1††</sup>, Sebastian H. Schmitt<sup>1</sup>, Zhujun Yu<sup>1</sup>,  
5 Robert Wegener<sup>1</sup>, Martin Kaminski<sup>1</sup>, Rupert Holzinger<sup>3</sup>, Armin Wisthaler<sup>2,5</sup>, Astrid Kiendler-Scharr<sup>1</sup>  
6

7 <sup>1</sup> Institute of Energy and Climate Research, IEK-8: Troposphere, Forschungszentrum Jülich GmbH, Jülich, Germany

8 <sup>2</sup> Institut für Ionenphysik und Angewandte Physik, Universität Innsbruck, Innsbruck, Austria

9 <sup>3</sup> Institute for Marine and Atmospheric research Utrecht, Princetonplein 5, 3584 CC, Utrecht, The Netherlands

10 <sup>4</sup> Ionicon Analytik GmbH, Innsbruck, Austria

11 <sup>5</sup> Department of Chemistry, University of Oslo, Norway

12

13 <sup>†</sup> Now at: German Environment Agency, Dessau-Roßlau, Germany

14 <sup>††</sup> Now at: Institute of Physics, University of Sao Paulo, Sao Paulo, Brazil

15

16 Correspondence to: T. Hohaus (t.hohaus@fz-juelich.de)

## 17 **Abstract.**

18 Secondary organic aerosols (SOA) play a key role in climate change and air quality. Determining the fundamental  
19 parameters that distribute organic compounds between the phases is essential, as atmospheric lifetime and impacts change  
20 drastically between gas- and particle-phase. In this work, gas-to-particle partitioning of major biogenic oxidation products  
21 was investigated using three different aerosol chemical characterization techniques. The aerosol collection module (ACM),  
22 the collection thermal desorption unit (TD) and the chemical analysis of aerosol on-line (CHARON) are different aerosol  
23 sampling inlets connected to a Proton Transfer Reaction-Time-of-Flight-Mass Spectrometer (PTR-ToF-MS). These  
24 techniques were deployed at the atmosphere simulation chamber SAPHIR to perform experiments on the SOA formation and  
25 aging from different monoterpenes ( $\beta$ -pinene, limonene) and real plant emissions (*Pinus sylvestris* L.). The saturation mass  
26 concentration  $C^*$  and thus the volatility of the individual ions was determined based on the simultaneous measurement of  
27 their signal in the gas- and particle-phase.

28 A method to identify and exclude ions affected by thermal dissociation during desorption and ionic dissociation in the  
29 ionization chamber of the PTR-MS was developed and tested for each technique. Narrow volatility distributions with organic  
30 compounds in the semi-volatile (SVOCs) to intermediate volatility (IVOCs) regime were found for all systems studied.  
31 Despite significant differences in the aerosol collection and desorption methods of the PTR based techniques, comparison of  
32 the  $C^*$  values obtained with different techniques were found to be in good agreement (within 1 order of magnitude) with  
33 deviations explained by the different operating conditions of the PTRMS.

34 The  $C^*$  of the identified organic compounds were mapped onto the 2-dimensional volatility basis set (2D-VBS) and results  
35 showed a decrease of the  $C^*$  with increasing oxidation state. For all experiments conducted in this study, identified  
36 partitioning organic compounds accounted for 20-30 % of the total organic mass measured from an AMS. Further  
37 comparison between observations and theoretical calculations was performed for species found in our experiments that were  
38 also identified in previous publications. Theoretical calculations based on the molecular structure of the compounds showed,  
39 within the uncertainties ranges, good agreement with the experimental  $C^*$  for most SVOCs, while IVOCs deviated up to a  
40 factor of 300. These latter differences are discussed in relation to two main processes affecting these systems: (i) possible  
41 interferences by thermal and ionic fragmentation of higher molecular weight compounds, produced by accretion and  
42 oligomerization reactions, that fragment in the  $m/z$  range detected by the PTRMS and (ii) kinetic influences in the  
43 distribution between gas- and particle-phase with gas-phase condensation, diffusion in the particle-phase and irreversible  
44 uptake.

## 45 1 Introduction

46 Secondary organic aerosol (SOA), formed by chemical reactions in the atmosphere, constitute a major fraction of the organic  
47 aerosol ((OA); Jimenez et al 2009)) and thus play a key role in climate change and air quality. A detailed understanding of  
48 SOA formation and composition is critical to develop strategies for impact mitigation (Volkamer et al., 2006;de Gouw et al.,  
49 2008;Hallquist et al., 2009;Jimenez et al., 2009). Defining the fundamental parameters that distribute organic molecules  
50 between the gas and particle phases is essential, as atmospheric lifetime and impacts change drastically between phases. The  
51 saturation vapor pressure (Pankow, 1994) and the enthalpies of vaporization and sublimation are key thermodynamic  
52 properties describing the gas-to-particle partitioning of organic compounds. Since SOA consists predominantly of oxidized  
53 multifunctional compounds (McFiggans et al., 2010) they are expected to show low saturation vapor pressures, thus  
54 increasing the detection challenges due to the low gas-phase concentrations that need to be probed (Bilde et al., 2015).

55 Advanced instrumentation for defining the saturation vapor pressure and thus the volatility of single component and complex  
56 organic aerosol systems has been developed in the past decades both for laboratory and field studies. Dicarboxylic acids  
57 represent a class of low-volatility compounds commonly found in atmospheric aerosol that are commercially available.  
58 These molecules have been extensively studied by various techniques (Bilde et al., 2015). Namely, the Knudsen effusion  
59 mass spectrometry (KEMS) (Booth et al., 2009) is a method where macroscopic crystalline samples effuse in a Knudsen cell  
60 and the change of the concentration in the gas-phase is measured using a mass spectrometer and translated to saturation  
61 vapor pressure values based on calibrated standards. Single particle methods using optical tweezers (Mitchem and Reid,  
62 2008) and the electrodynamic balance (EDB) (Pope et al., 2010) infer saturation vapor pressure values from the evaporation  
63 or condensational growth of a single particle at a controlled environment. Thermal desorption mass spectrometry (TDMS)  
64 has extended the studies from laboratory to ambient complex polydisperse systems. Thermodenuders have been extensively  
65 used to quantify the volatility of the bulk OA (An et al., 2007;Huffman et al., 2008;Faulhaber et al., 2009;Gkatzelis et al.,  
66 2016;Louvaris et al., 2017;Isaacman-VanWertz et al., 2017) with the support of model calculations (Riipinen et al.,  
67 2010;Karnezi et al., 2014). However, the detector used in most of these studies is an Aerosol Mass Spectrometer (AMS)  
68 (Canagaratna et al., 2007) that operates at high vaporizer temperatures (600 °C) and ionizes the analytes by electron impact  
69 (70 eV) thus introducing excessive thermal and ionic dissociation.

70 Recently, several different methods have been developed that compromise between molecular level information for a small  
71 fraction of the OA mass (Williams et al., 2006;Kreisberg et al., 2009;Hohaus et al., 2010;Williams et al., 2014;Zhang et al.,  
72 2014) or chemical formula identification using soft ionization MS to achieve a nearly full OA characterization (Lopez-  
73 Hilfiker et al., 2014;Isaacman-VanWertz et al., 2017;Stark et al., 2017;Gkatzelis et al., 2018). Volatility measurements are  
74 performed either by calibrating with standards of known saturation vapor pressure (Lopez-Hilfiker et al., 2014;Lopez-  
75 Hilfiker et al., 2015) or by simultaneous measurement of the gas- and particle-phase of an ion (Hohaus et al.,  
76 2015;Isaacman-VanWertz et al., 2016;Stark et al., 2017).

77 In order to identify the OA on a molecular level, thermal desorption techniques have been coupled to Gas-Chromatography  
78 (GC) methods. The Thermal Desorption Aerosol Gas Chromatograph/Mass Spectrometer (2D-TAG) (Goldstein et al., 2008)  
79 and the Volatility and Polarity Separator (VAPS) (Martinez et al., 2016) are similar techniques that provide volatility- and  
80 polarity-resolved OA information by using a 2-dimensional gas chromatography (2D-GC) approach. Volatility is derived  
81 based on the two-dimensional chromatographic retention times relative to those of known standards, thus establishing a  
82 retention time correlation (RTC) to the vapor pressure. Simultaneous measurements of the gas- and particle-phase mass of  
83 organic molecules has also been recently developed using the TAG system sampling alternately with and without a gas phase  
84 denuder in front of the inlet (Zhao et al., 2013b) and the modified semi-volatile TAG (SV-TAG) that utilizes two TAG cells  
85 in parallel (Isaacman-VanWertz et al., 2016). Although the above GC methods provide chemical speciation and gas-to-  
86 particle partitioning in a molecular level, they can only do so for a small fraction of the OA mass (10 – 40 %) (Williams et  
87 al., 2006;Williams et al., 2016).

88 Measurements using instrumentation to provide molecular identification (e.g. SV-TAG) or instrumentation for the  
89 identification of ions (e.g. different Chemical Ionization Mass Spectrometer (CIMS)) can be combined to increase the  
90 understanding of partitioning of some compounds classes. This was shown in an field intercomparison investigating gas-  
91 particle partitioning of oxygenated VOCs during the Southern Oxidant and Aerosol Study (SOAS) (Thompson et al., 2017).  
92 Newly developed thermal desorption inlets have allowed near-simultaneous chemical characterization of gas- and particle-  
93 phase ambient compounds (Holzinger et al., 2010;Lopez-Hilfiker et al., 2014;Yatavelli et al., 2014;Eichler et al., 2015;Stark  
94 et al., 2017;Gkatzelis et al., 2018). When coupled to chemical ionization high resolution time-of-flight mass spectrometers  
95 (ToF-CIMS) these inlets can provide information on a very broad volatility range (Eichler et al., 2017). By simultaneous  
96 measurement of the gas- and particle-phase mass concentration when applicable, direct volatility calculations of individual  
97 species can be performed. Indirect ways of estimating the vapor pressure for this type of systems has been also established  
98 based on the desorption temperature of calibrated known species or mixtures (Lopez-Hilfiker et al., 2016;Stark et al., 2017).  
99 Since the above mass spectrometric techniques can provide elemental formulas, methods to derive the vapor pressure by  
100 assuming a functional group composition have also been widely used (Pankow and Asher, 2008;Krechmer et al.,  
101 2015;Daumit et al., 2013;Li et al., 2016). A detailed comparison of the three different methods of estimating the vapor  
102 pressure for this type of techniques has been performed for field studies under forested areas (Stark et al., 2017). Results  
103 suggested that thermal decomposition pathways could bias the direct partitioning calculation based on the gas- and particle-  
104 phase concentrations as well as calculations based on the chemical formula of the species detected. Detailed understanding  
105 on the decomposition pathways is to be determined in future studies.

106 There are two major ways established in the last years to treat partitioning for practical applications to atmospheric aerosol.  
107 One is through a thermodynamic model containing an ensemble of specific molecules while the other is based on empirical  
108 calculations (Donahue et al., 2014). When using explicit methods, model systems are treated as fully as possible thus  
109 individual vapor pressures and activity coefficients are calculated based on several thermodynamic schemes (Fredenslund et  
110 al., 1975;Clegg et al., 2001;Zuend et al., 2011). These calculations are strongly affected by the wide range of vapor pressure  
111 estimates from the different theoretical approaches (Camredon et al., 2010;Donahue et al., 2014), thus further promoting the  
112 need of future development in this field. On the contrary, empirical methods tend to simulate gas-to-particle partitioning  
113 based on fits of partitioning data derived from chamber observations. Frameworks like the 2-Dimensional Volatility Basis  
114 Set (2D-VBS) classify OA in terms of bulk chemical characteristics and volatility (Donahue et al., 2012;Donahue et al.,  
115 2013). A variety of the above newly developed techniques can be mapped onto the 2D-VBS and thus provide important  
116 experimental input to further develop and test both the empirical methods and the newly developed instrumentation.

117 Deviations between the theoretical and experimental vapor pressure estimates are systematically observed (Bilde et al.,  
118 2015). Recent measurements show enrichment of semi-volatile organic compounds in the particle- relative to the gas-phase  
119 than calculations based on equilibrium vapor pressure would suggest (Zhao et al., 2013a;Hohaus et al., 2015;Isaacman-  
120 VanWertz et al., 2016). It is currently unclear whether this is due to (i) uncertainties in the theoretical estimates of vapor  
121 pressures, (ii) thermal decomposition pathways affecting the experimental partitioning determination or (iii) the existence of  
122 uptake pathways to particles other than absorption e.g. adsorption or reactive uptake. The wide range of theoretical vapor  
123 pressure estimates combined with the large gas-to-particle partitioning discrepancies of the above techniques (Thompson et  
124 al., 2017) promote further studies in order to bridge the gap between theory and experiments.

125 In this study, the gas-to-particle partitioning of major biogenic SOA (BSOA) oxidation products was investigated. An inter-  
126 comparison was performed using three different inlet techniques connected to soft-ionization mass spectrometry, the Aerosol  
127 Collection Module (ACM) (Hohaus et al., 2010), the Chemical Analysis of Aerosol Online (CHARON) (Eichler et al., 2015)  
128 and the Collection Thermal Desorption Cell (TD) (Holzinger et al., 2010). Volatility measurements were derived based on  
129 the mass concentration of individual species in the gas- and particle-phase, implemented in the 2D-VBS and compared to  
130 various explicit methods.

## 131 2 Methods and instrumentation

### 132 2.1 Facilities

133 The SAPHIR chamber is an atmospheric simulation chamber made of a double walled Teflon (FEP) foil with a volume of  
134 270 m<sup>3</sup>. It has a cylindrical shape and is housed in a steel frame. A shutter system mounted on the steel frame allows  
135 experiments to be conducted in the dark or when opened exposes the chamber to natural sunlight to initiate photochemistry.  
136 The pressure inside the chamber is kept at about 50 Pa overpressure compared to ambient pressures to ensure no diffusion  
137 from trace gases from the outside into the chamber. Additionally, the interspace of the double walled Teflon film is  
138 continuously flushed with pure nitrogen (Linde, purity 99.9999 %). A continuous flow of ultra clean air into the chamber  
139 compensates any losses due to leakages and ensures stable pressure conditions.

140 In preparation for each experiment the chamber is flushed with a high flow of up to 250 m<sup>3</sup>/h for several hours using the  
141 ultra-clean air. The same high flow rate is used to humidify the chamber before the start of each experiment. For  
142 humidification Milli-Q water is boiled and the steam is added to the air stream into the chamber. Two fans mounted inside  
143 the chamber generate well mixed starting conditions and were turned off as soon as aerosol production was initiated to reduce  
144 aerosol losses in the chamber. Ozone is added using a silent discharge ozonizer. Standard instrumentation is continuously  
145 measuring the conditions inside the SAPHIR chamber. Instrumentation includes an ultrasonic anemometer (Metek USA-1,  
146 accuracy 0.3 K) to measure the air temperature, a frost point hygrometer (General Eastern model Hygro M4) to determine  
147 the humidity, and a chemiluminescence analyser (ECO PHYSICS TR480) equipped with a photolytic converter (ECO  
148 PHYSICS PLC760) to measure NO and NO<sub>2</sub>. Ozone is measured by an UV absorption spectrometer (ANSYCO model  
149 O341M). Further details of the SAPHIR chamber are described in Rohrer et al. (2005).

150 Precursor compounds were added using two separate methods. The first method was to inject pure liquid compounds via a  
151 syringe in a heated inlet line, into the air stream with which the vapors were transported into the chamber. The second  
152 method was to use the plant chamber SAPHIR-PLUS (Hohaus et al., 2016) to transfer the emissions of six *Pinus sylvestris L.*  
153 (scots pine) into the chamber. Injection flow from SAPHIR-PLUS was 6 m<sup>3</sup>/h which replaced to a large extent the flow of  
154 clean air (8 m<sup>3</sup>/h) which is needed to replace air lost due to leakage and withdrawal of analytical instrumentation. The  
155 environmental parameters of the plant chamber are fully controlled (e.g., temperature, soil relative humidity,  
156 photosynthetically active radiation). The average temperature inside the SAPHIR-PLUS chamber was 25 °C. Details on the  
157 SAPHIR-PLUS are provided in Hohaus et al. (2016).

### 158 2.2 Instrumentation

159 All instruments used in this study are described in detail in Gkatzelis et al. (2018) and only a brief overview is provided in  
160 the following. An Aerodyne High-Resolution Aerosol Mass Spectrometer (HR-AMS) (DeCarlo et al., 2006; Canagaratna et  
161 al., 2007) and a Scanning Mobility Particle Sizer (SMPS, TSI Classifier model 3080, TSI DMA 3081, TSI Water CPC  
162 3786), were used to determine the aerosol chemical composition including the total organic mass concentration and the size  
163 distribution during the experiments, respectively. In order to determine the saturation mass concentrations (C\*) parallel gas-  
164 and particle-phase measurements were performed. Particle-phase composition was measured using three different aerosol  
165 sampling techniques coupled to a Proton-Transfer-Reaction Time-of-Flight Mass Spectrometer (model PTR-TOF 8000;  
166 PTR-ToF-MS, Ionicon), the Aerosol Collection Module (ACM-PTR-ToF-MS, referred to as “ACM” hereafter) (Hohaus et  
167 al., 2010), the chemical analysis of aerosol online (CHARON-PTR-ToF-MS, referred to as “CHARON” hereafter) (Eichler  
168 et al., 2015) and the collection thermal desorption unit (TD-PTR-ToF-MS, referred to as “TD” hereafter) (Holzinger et al.,  
169 2010). In the following, the most important characteristics and parameters are described briefly. The CHARON inlet  
170 combines a gas phase denuder, an aerodynamic lens with an inertial sampler and a thermodesorption unit which is coupled to  
171 a PTR-ToF-MS. The gas phase denuder removes gas phase analytes. Subsequently the aerosols are collimated by the

172 aerodynamic lens and a particle enriched sample flow is achieved by the inertial sampler. Afterwards the particles pass  
173 through a thermal desorption unit in which the particles are volatilized before transferred to the gas phase detector. The  
174 ACM has two sample air inlets. For the gas phase inlet air passes through a PTFE particle filter and is then directly  
175 introduced into the PTR-MS. For particle collection via the second sampling line air is passing through an aerodynamic lens  
176 removing gas phase and collimating particles onto a beam. The particles are subsequently passing a vacuum chamber and are  
177 collected on a cooled sampling surface. Once collection is finished particles are desorped and transferred via a carrier gas  
178 ( $N_2$ ) to the PTR-ToF-MS detector. Important to note is that during the collection process the PTR-ToF-MS is measuring the  
179 gas phase in parallel allowing for quasi simultaneous characterization of gas and particle phase. The TD also employs a gas  
180 phase denuder to remove gas phase analytes before the aerosols are impacted using a Collection and Thermo-Desorption  
181 (CTD) cell. After collection particles are thermally desorped and the components transferred to the PTR-ToF-MS. In the  
182 following, operational parameters are listed for all PTR-based instruments. The CHARON is a real time measurement (10 s  
183 integration time in the detector), while the ACM and TD have sampling times for this study of 120 min and 240 min,  
184 respectively. The CHARON inlet was operated at low pressure ( $< 1$  atm) and at a constant temperature of  $140$  °C. The  
185 sampling in the ACM was under vacuum conditions and at sub-zero temperature ( $-5$  °C). The sampling in the TD was at  
186 ambient temperature and at atmospheric pressure. The CHARON used a gas-phase denuder to strip off gas-phase compounds  
187 while the AMS-type vacuum inlet system of the ACM ensured a removal of the gas-phase. While the particle-phase in the  
188 CHARON was desorbed by passing particles through a thermodenuder, the particle-phase in the ACM and TD was desorbed  
189 after collection from the collection surface using a temperature ramp reaching a final temperature of  $250$  °C and  $350$  °C,  
190 respectively. All three aerosol collection techniques are utilizing a PTR-ToF-MS as a detector. The operational conditions  
191 for each PTR-ToF-MS were different with regard to a different electric field strength ( $V\ cm^{-1}$ ) to buffer gas density  
192 (molecules  $cm^{-3}$ ) ratio ( $E/N$ ). This can lead to different ionic fragmentation behavior. Therefore the overlap of parent ions  
193 measured between the different instruments can be reduced. A detailed discussion about the  $E/N$  effect has been investigated  
194 by Gkatzelis et al. (2018). Operational details for the different PTR-ToF-MS conditions are given also in Table S2. The  
195 PTR-ToF-MS of the CHARON, ACM, and TD were operated at 100 Td, 120 Td, 160 Td, respectively ( $1\ Td = 10^{17}\ V\ cm^2$   
196  $molecule^{-1}$ ). The drift tube conditions for the PTR-ToF-MS of CHARON, ACM, and TD were at a temperature of  $100$  °C  
197 with a pressure of 2.30 mbar,  $120$  °C and a pressure of 2.40 mbar, and  $120$  °C and a pressure of 2.40 mbar, respectively. The  
198 limit of detection (LOD), depended on the different pre-concentration factors for each technique, which resulted in TD  
199 having the lowest LOD ( $10^{-3}\ ng\ m^{-3}$ ), followed by the CHARON ( $1.4\ ng\ m^{-3}$ ), while ACM showed the highest values  
200 ( $250\ ng\ m^{-3}$ ). Finally, differences in sensitivity for each PTR-MS introduced minor deviations in this study and are discussed  
201 in detail in Gkatzelis et al., (2018). A characteristic timeseries of a major oxidation product from the  $\beta$ -pinene ozonolysis for  
202 the three different techniques can be found in Figure S8.

203 Gas-phase organic compounds were detected by a standalone PTR-ToF-MS for the CHARON and TD. The standalone PTR-  
204 ToF-MS was operated with an  $E/N = 120$  Td. The drift tube was kept at a temperature of  $60$  °C and a pressure of 2.30 mbar.  
205 The standalone PTR-MS was connected to SAPHIR via a 0.5 m PFA line (inner diameter, i.d. 3.2 mm), to a 2 m PEEK line  
206 (i.d. 1 mm), heated at  $60$  °C with a flow of  $0.6\ L\ min^{-1}$  that resulted to an overall residence time of  $\sim 0.6$  s. The ACM was  
207 connected via a 4 m PFA line (i.d. 4 mm), at room temperature with a flow of  $0.7\ L\ min^{-1}$ , resulting to a residence time of  
208 approximately 3 s. A PTFE particle filter (Merck Millipore) was additionally introduced to the PTR-MS line of the ACM to  
209 reassure complete particle-phase removal. Gas-phase compounds were then directed to the ACM-PTR-MS interface that was  
210 heated at  $280$  °C via a 5 cm coated stainless steel line (i.d. 0.8 mm) to the PTR-MS. The ACM design allowed for  
211 simultaneous gas-phase measurements with the same PTR-ToF-MS while sampling of the particle-phase took place on the  
212 ACM collector. Comparison of gas and particle-phase measurements was thus performed using the same detector avoiding  
213 any detector related differences. It should be noted that TD and CHARON are also designed for simultaneous gas- and  
214 particle-phase measurements using the same PTR-MS but in this study this feature was not operational.

### 215 2.3 Experimental conditions

216 Before each experiment the SAPHIR chamber was flushed with clean air over night (total volume exchange was about 2000  
217 m<sup>3</sup>) and humidified directly after the flushing process. Relative humidity (RH) in the chamber was about 55 % within a  
218 temperature range for all experiments between 295 K and 310 K. After ensuring that all instruments had measured the  
219 background in the SAPHIR chamber a single monoterpene ( $\beta$ -pinene or limonene), a monoterpene mixture ( $\beta$ -pinene and  
220 limonene) or the emissions of 6 *Pinus sylvestris* L. (Scots pine) were injected. The tree emissions were characterized using  
221 GC-MS. The composition of the biogenic VOC (BVOC) consisted of 42%  $\delta^3$ -carene, 38%  $\alpha$ -pinene, 5%  $\beta$ -pinene, 4%  
222 myrcene, 3% terpinolene and 8% other monoterpenes. The details of all experiments are given in Table 1 and an  
223 experimental overview is provided in Figure S1. One hour after injection of the VOCs ozone was introduced into the  
224 chamber to initiate ozonolysis with the subsequent formation of secondary organic aerosols (SOA). Experiments were done  
225 without the use of an OH scavenger. NO<sub>x</sub> concentrations during the experiments ranged between 10 to 60 pptv originating  
226 from HONO background source (Rohrer et al., 2005). In all experiments, except for the experiment with limonene as a  
227 precursor, 20 hours after the start of the ozonolysis the roof of the SAPHIR chamber was opened to initiate additional  
228 photochemistry with OH and ageing of the SOA. For the limonene experiment instead of opening the roof, 30 ppbv of NO  
229 was added to the chamber. With the remaining ozone in the chamber, NO<sub>3</sub> oxidation was initiated. In the tree emissions  
230 experiment the SAPHIR-PLUS chamber was recoupled to the SAPHIR chamber 11 hours after the start of the ozonolysis  
231 thus injecting again fresh BVOC emissions from the scots pines. The experiment continued for an additional 6 hours with the  
232 roof open allowing for further oxidation of the BVOCs and SOA by OH radicals. The duration of the experiments varied  
233 from 17 to 36 hours, providing ample time to experimentally investigate the aging of the biogenic SOA.

234

### 235 2.4 Estimation of volatility distribution

236 In this work the volatility of different species was quantified based on their saturation mass concentration C\* in units of  
237  $\mu\text{g m}^{-3}$ . Theoretical calculation of the saturation concentration was performed for known oxidation products of the  
238 monoterpenes studied based on their chemical structure as seen in Table S1. Based on the absorption equilibrium partitioning  
239 formalism, the (sub-cooled liquid) saturation vapor pressure ( $p_{i,L}$ ) of a species was related to its C\* based on Cappa and  
240 Jimenez (2010) as following:

$$241 \quad C^*(T) = \frac{MW_{OA} \times 10^6 \times p_{i,L} \times \zeta_i}{R \times T} \quad (1)$$

242 where MW<sub>OA</sub> is the molecular weight of the condensed organic phase (g mol<sup>-1</sup>),  $p_{i,L}$  is the sub-cooled liquid saturation vapor  
243 pressure (Pa),  $\zeta_i$  is the activity coefficient of species i in the OA phase, T is the chamber temperature (K) and R is the ideal  
244 gas constant (8.314 J mol<sup>-1</sup> K<sup>-1</sup>). Here, the calculations were performed using a mean molecular weight of 180 g mol<sup>-1</sup> (Prisle  
245 et al., 2010). In conformity with Donahue et al. (2014) the activity coefficients of all considered species partitioning into a  
246 mixed aerosol system containing similar compounds were assumed to be 1 throughout the study.

247 At present, there is a scarcity of reliable saturation vapor pressure data obtained through laboratory studies (Bilde et al.,  
248 2015). Therefore,  $p_{i,L}$  is commonly estimated using empirical relationships derived from the Clausius-Clapeyron equation  
249 e.g. (Myrdal and Yalkowsky, 1997; Jenkin, 2004; Nannoolal et al., 2008). The required thermodynamic properties, such as the  
250 boiling temperature or the enthalpy of vaporization are predicted from the molecular structure of the investigated compounds  
251 (Mackay et al., 1982; Joback and Reid, 1987; Stein and Brown, 1994). Their explicit manual calculation using the existing  
252 functional group contribution methods are very laborious not only because of the high number of components, but also  
253 because of the wide range of multifunctional organic compounds in the aerosol mixtures. Recently, a new web-based facility,  
254 UManSysProp (<http://umansysprop.seaes.manchester.ac.uk>), was developed for automating predictions of i.e. pure  
255 component vapor pressures of organic molecules or activity coefficients for mixed liquid systems. For the group contribution

256 approaches, only the molecular information must be uploaded in form of SMILES (Simplified Molecular Input Line Entry  
257 System) strings (Toppings et al., 2016). At a defined temperature, there are several options for vapor pressure predictive  
258 techniques, providing the possibility to combine two different empirical representations of the Clausius-Clapeyron equation  
259 (Myrdal and Yalkowsky, 1997;Nannoolal et al., 2008) - further referred to as MY and NN, respectively - with three different  
260 prediction methods for thermodynamic properties of the investigated compound based on their molecular structure (Joback  
261 and Reid, 1987;Stein and Brown, 1994;Nannoolal et al., 2008) - further referred to as JR, NN and SB, respectively.  
262 Additionally, the EVAPORATION method (further referred to as EVAP) proposed by Compernelle et al. (2010) is available  
263 for the web-based calculations.

264 Here, we use the  $p_{i,L}$  predicted online by UManSysProp facility, examining all seven estimation methods (Figure S6 and S7).  
265 Only the results giving the lowest and highest vapor pressures for the studied compounds (the range of the estimates are  
266 indicated by the grey background color) are used in this study to compare measurements to the highest and lowest possible  
267 theoretical values.

268 Experimental determination of the saturation mass concentration of the individual compounds was derived by applying the  
269 partitioning theory (Pankow, 1994) based on Donahue et al. (2006) as

$$270 \quad C^* = OA \times \frac{G_i}{P_i} \quad (2)$$

271 where OA is the total organic mass ( $\mu\text{g m}^{-3}$ ) determined from AMS and  $G_i$  and  $P_i$  are the gas- and particle-phase mass  
272 concentration ( $\mu\text{g m}^{-3}$ ) of compound  $i$ , respectively, measured from the PTR based techniques. Assuming typical  
273 vaporization enthalpies (e.g.  $\Delta H^{\text{VAP}}=127 \text{ kJ mol}^{-1}$ ) (Epstein et al., 2010),  $C^*$  and therefore partitioning is strongly dependent  
274 on temperature with changes of  $\pm 15 \text{ }^\circ\text{C}$  resulting in a  $C^*$  change by a factor of 10. During the campaign the average  
275 chamber temperatures and their standard deviations were  $20 \pm 4 \text{ }^\circ\text{C}$ ,  $17 \pm 4 \text{ }^\circ\text{C}$ ,  $19 \pm 5 \text{ }^\circ\text{C}$  and  $30 \pm 5 \text{ }^\circ\text{C}$  for the  $\beta$ -pinene,  
276 limonene, mixture and trees experiment, respectively. The uncertainty added from these variations ( $< 10 \text{ }^\circ\text{C}$ ) was further  
277 examined with a focus on the  $\beta$ -pinene oxidation products (Figure S7). Difference in volatility due to variations ranged from  
278 0.3 to 0.6  $\log(C^*)$  depending on the chemical structure of the compound. Nevertheless, these variations can be considered  
279 small and not strongly affecting the conclusions of this work. Therefore, for consistency with other studies, a reference  
280 temperature of 298 K was used throughout all  $C^*$  calculations. This was recently proposed by Stark et al. (2017) to derive  
281 the average  $C^*$  for the BEACHON and SOAS field campaigns making the assumption that deviations due to temperature  
282 changes ( $18 \pm 7 \text{ }^\circ\text{C}$  and  $25 \pm 3 \text{ }^\circ\text{C}$ , respectively) were within the uncertainties of the measurements. Calculation of the  
283 average  $C^*$  for each experiment was performed based on the time resolution of each instrument (section 2.2). When the  
284 signal in the particle-phase was close to the detection limit, introducing a high uncertainty, the calculation of the  $C^*$  was not  
285 performed.

286

## 287 3 Results and discussion

### 288 3.1 Compound selection: Assessment of ionic and thermal decomposition

289 For all PTR based techniques the molecular formula  $(C_xH_yO_zN_a)H^+$  was attributed to each detected signal derived from the  
290 exact molecular mass which was determined by the TOF-MS. Whether the detected ion was an original SOA compound or a  
291 fragment detected on this mass could be affected by two major processes, (i) thermal dissociation during desorption, and (ii)  
292 ionic dissociation in the ionization region of the PTR-ToF-MS.

293 Thermal dissociation has been found to introduce a high degree of fragmentation for compounds that contain multiple  
294 functional groups, including peroxide groups which are thermally labile (Lopez-Hilfiker et al., 2015). For organic alcohols  
295 and acids thermal desorption has been shown to lead to loss of carboxyl- ( $-\text{CO}_2$ ), carbonyl- ( $-\text{CO}$ ) and water-groups ( $-\text{H}_2\text{O}$ )

296 (Canagaratna et al., 2015). Accretion reactions and gas-phase autoxidation have been found to play a key role in extremely  
297 low volatility OC (ELVOC) formation (Tobias and Ziemann, 1999, 2001; Ehn et al., 2014). Upon heating, such products will  
298 thermally decompose (Barsanti et al., 2017) and be detected in the lower molecular weight range, thus directly affecting the  
299 partitioning estimation (Jang and Kamens, 2001; Stark et al., 2017). All instruments deployed in this study were subjected to  
300 possible thermal dissociation with decarboxylation and dehydration reactions strongly dependent on the temperature,  
301 pressure and the heat exposure time of the molecules during desorption. CHARON was operated at the lowest temperature of  
302 140 °C, under a few mbars of pressure and with the lowest heat exposure time, therefore minimizing the latter reactions.  
303 ACM and TD were operated at 1 bar and up to 250 °C and 350 °C, respectively, with longer heat exposure times.  
304 Functional group loss has been found to additionally occur in the ionization region of the PTR-ToF-MS instruments.  
305 Gkatzelis et al. (2018) showed that for this study the ratio of the electric field strength ( $V\text{ cm}^{-1}$ ) to buffer gas  
306 density ( $\text{molecules cm}^{-3}$ ) ( $E/N$ ) in the PTR-ToF-MS instruments played a key role in decomposition, not only due to water  
307 loss but also carbon-oxygen bond breakage of the detected molecules. Even though PTRMS is considered a soft ionization  
308 technique compared to e.g. AMS, these decomposition pathways could still lead to misidentification of the original chemical  
309 composition of the SOA species. For the ACM the ionic fragmentation for the gas- and particle-phase species was identical  
310 since both measurement were conducted using the same PTR-ToF-MS as a detector. CHARON and TD saturation mass  
311 concentration ( $C^*$ ) was determined by using the gas-phase mass concentration measurements derived from a separately  
312 deployed PTR-ToF-MS operated at different  $E/N$  conditions (see Section 2.2). Ionic dissociation was thus different for the  
313 gas- compared to the particle-phase measurements increasing the uncertainty of the volatility estimation for CHARON and  
314 TD when compared to ACM.

315 A method to identify the ionic and thermal dissociation processes and their effect to the different techniques is presented in  
316 the following. This method was applied to the calculated average  $\log(C^*)$  of each ion, found both in the gas- and particle-  
317 phase, for each experiment for the individual instruments. A characteristic example of the  $\beta$ -pinene ozonolysis experiment  
318 (as shown in Figure 1) for the ACM is used here to explain this method. Information of the carbon (x-axis) and oxygen (size  
319 of the markers) atom number contained in the chemical formulas were used to differentiate between the different ions  
320 (Figure 1a). Each marker indicates one ion, therefore for the  $\beta$ -pinene experiment 72 ions were detected both in the gas- and  
321 particle-phase by the ACM. Their average saturation mass concentration  $\log(C^*)$  and therefore their volatility ranged from  
322  $10^1$  to  $10^4\ \mu\text{g m}^{-3}$ , an indication of semi-volatile and intermediate-volatile species in the SOA mass. From these ions, 55 were  
323 identified as fragmentation products accounting for 70 % of the partitioning ions and only 25 % of these ions were used for  
324 further analysis.

325 Two major criteria were applied to differentiate between a possible parent ion (green markers) and a fragment. The first  
326 criteria was if the carbon and oxygen atom number were lower than 6 and 1, respectively. This criteria was chosen based on  
327 Donahue et al. (2006) who have shown that organic aerosols are expected in the range from ELVOC to SVOC and IVOC  
328 with saturation concentrations ranging from -5 to 4. This volatility regime consists of species with carbon and oxygen atom  
329 numbers equal or larger than 6 and 1, respectively (Donahue et al., 2011; Donahue et al., 2012). Ions found in the particle-  
330 phase with lower carbon and oxygen numbers were thus considered fragmentation products (grey markers) and were not  
331 used in the analysis. The second criteria focused on the dependence of the volatility to the number of oxygen and carbon  
332 atoms that constitute an organic molecule. As the oxygen and carbon atom number and thus the functionality of the molecule  
333 increased, the saturation mass concentration was expected to decrease (Pankow and Barsanti, 2009). If the volatility of an  
334 identified ion  $[M+H]^+$  was identical to (within an uncertainty of  $\log(C^*) \pm 0.25$ ) or higher than the volatility of ions with the  
335 same chemical formula subtracting a functional group  $[M+H-FG]^+$  the latter were considered highly affected by either ionic  
336 or thermal dissociation and were excluded from further analysis. Characteristic examples of this analysis are shown in Figure  
337 1b and c. The y-axis corresponded to identified ions  $[M+H]^+$  while the x-axis to ions with the same chemical formula  
338 subtracting water ( $-H_2O$ ) (Figure 1b) or a carbonyl group ( $-CO$ ) (Figure 1c). When the ions  $[M+H]^+$  and  $[M+H-FG]^+$  were



339 found to have identical saturation concentrations,  $[M+H-FG]^+$  ions were excluded (blue and orange markers in Figure 1b and  
340 c, respectively).  $[M+H-FG]^+$  ions that showed lower volatility when compared to  $[M+H]^+$  ions were considered fragments of  
341 unknown decomposition pathways (i.e. unknown parent ion composition) and were excluded as well (yellow markers). Only  
342 when ions  $[M+H-FG]^+$  showed higher volatility values than  $[M+H]^+$  they were considered to be possible parent ions not  
343 strongly affected by thermal or ionic dissociation (green markers) and were further analyzed. The same comparison was not  
344 only performed for (-H<sub>2</sub>O) and (-CO) functional group loss but was extended to (-CO<sub>2</sub>), (-H<sub>2</sub>O<sub>2</sub>), (-H<sub>2</sub>O) plus (-CO), and (-  
345 H<sub>2</sub>O) plus (-CO<sub>2</sub>). Checks were also performed for loss of the (-HNO<sub>3</sub>) functional group for the limonene-NO<sub>3</sub> oxidation  
346 experiment but due to the high E/N operating conditions of all PTR-ToF-MS systems, no organic nitrates were identified  
347 (Duncan et al., 2017).

348 It should be noted that PTR-MS provides information regarding the chemical formula of an ion and thus disregards potential  
349 impact of the chemical structure. Functionality effect (e.g. stronger hydrogen bonding of an alcohol in a polar particle) can  
350 lead to a misidentification of potential parent ions as a fragment using the above described method due to the fact that a  
351 lower volatility is determined compared to an expected volatility based on the chemical formula. Nevertheless, although this  
352 method will potentially exclude parent ions, it will still discard also any possible fragments. Correlation analysis based on  
353 the time series of the different compounds could further improve the parent ion identification. However due to the low time  
354 resolution in this work a time series analysis is not applicable. Another implication relies on the fact that  $[M+H]^+$  ions could  
355 result from the decomposition of accretion reaction products or oligomers, consequently leading to an overestimation of their  
356 particulate phase concentrations. This effect is not constrained by this method and is further addressed in Section 3.4.  
357 Furthermore, although this method can efficiently eliminate possible fragments it does not provide proof that these fragments  
358 originate from the suggested fragmentation pathways. An overview of the fragmentation identification results of this method  
359 for each instrument and experiment are provided in Figure S2. Percentages are derived based on the total number of  
360 fragment ions and how they distribute (%) to the different fragmentation pathways. For all PTR based techniques 40 to 60%  
361 of the partitioning ions were detected below the carbon and oxygen atom number threshold of C<sub>6</sub> and O<sub>1</sub> respectively. From  
362 the remaining species, ions affected by water (-H<sub>2</sub>O) loss were around 5-10%, while carboxyl group (-CO<sub>2</sub>) fragmentation  
363 was identified for less than 10% of the partitioning ions. Loss of (-CO), (-H<sub>2</sub>O<sub>2</sub>), (-H<sub>2</sub>O) plus (-CO) and (-H<sub>2</sub>O) plus (-CO<sub>2</sub>)  
364 functional groups affected less than 5% of the ions for all experiments and instruments studied. Ions of unknown  
365 decomposition pathways represented  $\leq 10\%$  with TD showing the highest values. ACM showed increased contributions of  
366 lower molecular weight ions, compared to TD and CHARON, for limonene and mixture experiments (max 65%). In total,  
367 the fraction of ions identified as parent compounds partitioning in the gas- and particle-phase that were chosen for further  
368 analysis in the next sections ranged between 20-40% of the overall ions found in both phases, for each experiment and  
369 instrument studied.

370 The high contribution of lower MW ions found both in the gas- and particle-phase for all PTR-based techniques further  
371 supported that ionic and thermal dissociation played a key role in carbon-oxygen bond breakage. The higher E/N values of  
372 ACM and TD compared to CHARON resulted in higher fragmentation, thus higher contribution of the lower MW  
373 partitioning ions (Gkatzelis et al., 2018). Although ACM was operated at lower E/N conditions compared to TD, the  
374 contribution of lower MW ions was higher. The reason for this discrepancy was due to the higher limit of detection of the  
375 ACM (section 2.2) compared to TD and CHARON. Ions of low concentrations in the higher MW range that could be  
376 detected from CHARON and TD were below the detection limits of the ACM and were therefore not identified. For the  
377 remaining higher MW species, the water (-H<sub>2</sub>O) loss was the dominant fragmentation pathway for all techniques. Although  
378 the PTR-based techniques were operated at different temperature, desorption residence times and pressure conditions they  
379 showed similar percentage of ions affected by water loss. This is an indication that for all techniques dehydration occurred  
380 mostly due to ionic fragmentation in the ionization region of the PTRMS and not due to thermally initiated reactions for the  
381 partitioning ions studied. TD showed a higher contribution of fragments of unknown decomposition pathways when

382 compared to ACM and CHARON due to the highest difference of E/N operating conditions in the particle-phase (160 Td)  
383 compared to the gas-phase (120 Td), with the latter measured by a separately deployed PTR-ToF-MS. The higher ionic  
384 dissociation in the particle-phase increased the concentration of lower MW ions and decreased that of higher MW ions. This  
385 had a direct effect on the calculation of the volatility based on equation 2. When this effect was strong enough fragment ions  
386  $[M+H-FG]^+$  showed higher concentrations in the particle phase thus lower volatility when compared to possible parent ions  
387  $[M+H]^+$ . These ions were, based on this method, excluded as fragments of unknown fragmentation pathways and showed an  
388 expected higher contribution for systems like the TD. Fragment loss of  $(-CO_2)$ ,  $(-CO)$ ,  $(-H_2O_2)$ ,  $(-H_2O)$  plus  $(-CO)$  and  $(-$   
389  $H_2O)$  plus  $(-CO_2)$  accounted for 10% or less suggesting that these pathways were not dominating the partitioning ions  
390 studied. Interference of accretion reaction products or oligomers which could be detected at a lower m/z due to  
391 decomposition processes are not accounted for in the previous described method. Possible effect of such an interference is  
392 further discussed in Section 3.4.

393

### 394 3.2 Volatility distribution coverage

395 The mass concentrations of only the species identified as parent ions for ACM, CHARON and TD were distributed to  
396 different volatility bins ranging from  $\log(C^*)$  of -1 to 5 with a 0.5 bin volatility resolution. The normalized volatility  
397 distribution (NVD) for each experiment accounting for all PTR-based techniques is shown in Figure 2 (a, b, c, d).  
398 Normalization was performed by dividing each volatility bin by the sum of the PTR-based technique mass concentration  
399 measured at each experiment. The detected biogenic SOA partitioning species showed  $\log(C^*)$  values from 0 to 4, an  
400 indication that mainly SVOCs and IVOCs were predominantly measured simultaneously in the gas- and the particle-phase.  
401 The limonene  $NO_3$  oxidation experiment had the lowest NVD starting from a  $\log(C^*)$  of 0.5, with a narrow spread up to 2.  
402 For the  $\beta$ -pinene and  $\beta$ -pinene/limonene mixture experiments the NVD moved towards more volatile species ranging from  
403 0.5 to 4. When comparing the single compound experiment of  $\beta$ -pinene to the mixture, the latter showed a NVD shifted to  
404 lower saturation concentrations. Partitioning species detected from all the PTR-based techniques were further compared as  
405 seen in Figure 2 (e, f, g, h). ACM and CHARON showed same volatility values for all experiments with only the trees  
406 experiment resulting in higher deviations from the one to one line. TD presented higher  $\log(C^*)$  when compared to  
407 CHARON and ACM, suggesting the examined species were underestimated in the particle-phase. A total of 5, 2, 6 and 4  
408 ions were observed to partition with all three techniques for the  $\beta$ -pinene, limonene,  $\beta$ -pinene/limonene mixture and tree  
409 emissions experiment, respectively after applying the parent ion identification method of section 3.1.

410 Calculation of the  $\log(C^*)$  in this study relied on the ratio between the gas- and particle-phase signal of an ion (equation 2).  
411 Detection limits of both of these limited the measurable range of this ratio. This explains the narrow volatility distributions  
412 available with all PTR-based techniques, as has been previously reported by Stark et al. (2017). Combining the capabilities  
413 of these instruments and the above approach to calculate the volatility provided insights in a defined range of SVOCs and  
414 IVOCs. Within this volatility range the differences observed when using different precursors agrees with bulk volatility  
415 measurement findings that limonene SOA is less volatile than  $\beta$ -pinene SOA (Lee et al., 2011). When focusing on the  
416 species measured differences of ACM and CHARON to TD could be explained by the higher E/N conditions of TD that  
417 were previously discussed (section 3.1). Since TD was more prone to particle-phase fragmentation compared to the gas-  
418 phase these higher MW compounds showed lower concentrations, thus indicated higher volatility. This effect was negligible  
419 for ACM that was using the same PTRMS for gas- and particle-phase measurements and lower for CHARON operated at  
420 lower E/N conditions. The agreement of ACM and CHARON for all experiments except the trees experiment further  
421 promoted that both techniques measured the same species in good agreement and within the uncertainties of these  
422 calculations. As the complexity of the system increased, this agreement deviated from the one to one line. Gkatzelis et al.  
423 (2018) reported that for the single precursor and mixture experiments ions were detected with C6 to C12 carbon atoms from

424 all techniques. On the contrary, during the tree emissions experiment CHARON was the only instrument to detect ions in the  
425 C13 to C20 range. These ions were not detected from ACM or TD that were operated at higher E/N conditions and were  
426 more prone to ionic and thermal dissociation. Fragmentation of these higher carbon atom ions could affect the volatility  
427 calculation of lower MW species still detected by ACM and TD and thus explain the deviations seen for the tree emissions  
428 experiment.

429 The total number of species seen from all techniques was low due to the parent ion identification method applied in the  
430 previous section. An overview of the overlapping compounds is provided in Figure S3. When all detected ions were taken  
431 into account more than 50 ions were seen from all techniques at each experiment. After narrowing our focus on the  
432 partitioning ions and excluding the lower MW fragments the overlapping compounds dropped to ~ 15 ions. Each technique  
433 was affected differently by ionic and thermal dissociation. By applying the above method to each technique, different ions  
434 were excluded for each instrument thus leading to only a few species seen from all three techniques and accounted as parent  
435 ions.

436

### 437 **3.3 Experimentally derived saturation concentration implemented to the 2D-VBS**

438 Species identified as parent ions from each technique were combined and further analysed with a focus on their average  
439 saturation concentration as seen in Figure 3. For parent ions measured from more than one instrument, the average of all  
440 techniques was used to determine the overall experimental  $C^*$  of the ion, with the error bars indicating the error of this  
441 average. The 2D-VBS (Donahue et al., 2011; Murphy et al., 2012) framework was used to implement the results for each  
442 experiment with background colors corresponding to the different volatility classes, ranging from IVOCs (grey) to SVOCs  
443 (green) and LVOCs (red). It should be noted that the oxidation state ( $OS_C$ ) was not derived by bulk measurements using e.g.  
444 the AMS, but by using the  $OS_C$  of the individual species based on their carbon, hydrogen and oxygen atom number (Kroll,  
445 2011). In total 48, 31, 46 and 79 ions were identified as parent ions for the  $\beta$ -pinene, limonene,  $\beta$ -pinene/limonene mixture  
446 and tree emissions oxidation experiment, respectively. The saturation concentration showed a decrease for species with  
447 higher OS and oxygen atom number. For the limonene experiment lower saturation concentration values for compounds  
448 defined by the same oxidation state was found when compared to the  $\beta$ -pinene, mixture or tree emissions experiment.  
449 Overall, parent ions corresponded to 20-30 % of the overall organic mass measured from an AMS for all systems studied.

450 The observed volatility decrease with increasing OS and oxygen atom number is in good agreement with previous findings  
451 (Jimenez et al., 2009; Kroll, 2011). Lower volatility values for limonene species with the same OS when compared to the  $\beta$ -  
452 pinene, mixture or the tree emissions experiment suggested that species originating from different precursors and oxidation  
453 pathways with differences in their functionality and molecular structure affected their gas-to-particle partitioning. It should  
454 be noted that the lower volatility of limonene could be partly explained by the absence of TD measurement in this  
455 experiment and thus the absence of TD  $C^*$  values when averaging the experimental results from all PTR-based techniques.  
456 Since TD was affected the strongest by ionic dissociation (highest E/N), the  $C^*$  values were biased to higher volatilities  
457 when compared to ACM and CHARON with particle-phase measurements ( $P_i$  in equation 2) fragmenting more compared to  
458 the gas-phase ( $G_i$  from dedicated gas-phase PTR operated at lower E/N). Results when averaging all experiments and  
459 excluding the TD data are shown in Figure S4. Although the limonene experiment would still show lower volatilities  
460 compared to the  $\beta$ -pinene and mixture experiments this trend would be less strong suggesting that the absence of TD during  
461 the limonene experiment did lower the overall average volatility calculation presented in Figure 3. The increased number of  
462 species detected during the tree emissions experiment occurred due to the higher complexity of this system with more than  
463 one precursor oxidized to form SOA. In total, the PTR-based techniques showed that 20-30 % of the overall BSOA mass  
464 consisted of ions with volatilities within the SVOC to IVOC range further showing the importance of understanding the gas-  
465 to-particle partitioning and thermodynamic properties of compounds formed in such systems.

466 At this point, it should be noted that losses of gas-phase compounds through the lines, from the SAPHIR to the PTR-MS,  
467 could also affect the  $\log(C^*)$  calculation, by changing the ratio of the gas- to the particle-phase. Gas-phase measurements  
468 were performed using a standalone PTR-MS for TD and CHARON while for the ACM both gas- and particle-phase  
469 measurements were obtained using the same PTR-MS of ACM. The two PTR-MS differed in inlet length, temperature, and  
470 material with ACM-PTR-MS introducing higher residence times, thus longer exposure of the gas-phase compounds to the  
471 line walls (see Section 2.2). If significant losses of gas-phase compounds in the ACM-PTR-MS compared to the standalone  
472 PTR-MS line would occur, the gas-phase concentration would be underestimated and therefore also the  $\log(C^*)$  derived by  
473 the ACM measurements. To test if the dissimilarities between the different PTR-MS inlet lines are biasing the results of the  
474 ACM, re-calculation of the  $\log(C^*)$  was performed by using equation 2 and applying the ACM particle-phase concentration  
475 ( $P_i$ ), but changing the gas-phase concentration ( $G_i$ ) to measurements from the standalone PTR-MS. This calculation was  
476 performed for all ions identified as parent ions for the ACM when using the parent ion identification method. An overview  
477 of the correlation of the  $\log(C^*)$  using the two different gas-phase datasets is shown in Figure S5. For all experiments and for  
478 most of the compounds, agreement within the uncertainty of the measurements was found. For the tree emissions oxidation  
479 experiment the fraction of compounds deviating from the one to one line was higher. The spread in the data around the one  
480 to one line can be explained by the fact that though both PTR-MS were the same type of model differences in the e.g. the  
481 TOF interface and the drift tube existed. These differences affected the fragmentation and resolution of the PTR-MS  
482 (Gkatzelis et al., 2018) and could therefore explain the deviations observed. Moreover, the tree emissions experiment showed  
483 the highest complexity in comparison to the single precursor oxidation experiments, with detected ions that had up to 20  
484 carbon atoms in the particles. These higher molecular weight ions fragmented differently when passing through the differing  
485 ToF interfaces and thus resulted to the observed higher deviation. However the differences are within the experimental  
486 uncertainties and therefore no significant bias due to potential inlet line interference could be determined.

### 487 3.4 Experimentally derived saturation concentration compared to explicit methods

488 In order to derive further information from the experimentally determined parent ions, comparison to previous publications  
489 was performed for the major oxidation products from (a) the  $\beta$ -pinene ozonolysis (Yu et al., 1999; Jenkin, 2004; Chen and  
490 Griffin, 2005; Steitz, 2010; Kahnt, 2012; Hohaus et al., 2015), (b) limonene ozonolysis and  $\text{NO}_3$  oxidation (Chen and Griffin,  
491 2005; Leungsakul et al., 2005b; Leungsakul et al., 2005a; Jaoui et al., 2006; Kundu et al., 2012) and (c) tree emissions  
492 ozonolysis with  $\alpha$ -pinene and  $\Delta^3$ -carene being the major reactants (Yu et al., 1999; Chen and Griffin, 2005; Praplan et al.,  
493 2014). By attributing a chemical structure to the ions identified by the PTR-MS, detected parent ions that overlapped with  
494 compounds from previous publications were further examined based on their structural information. An overview of the  
495 overlapping compounds and their suggested structures are given in Table S1. Uncertainties introduced by assigning a  
496 chemical structure to an ion of a given chemical formula are further discussed in this section.

497 A detailed analysis of the  $\beta$ -pinene ozonolysis experiment was performed as seen in Figure 4. Experimental calculation of  
498 the saturation concentration was performed based on the average  $C^*$  values throughout the experiment when taking into  
499 account all PTR-based techniques with the error bars indicating the  $\pm 1\sigma$  of this averaging. The theoretical calculations by  
500 UManSysProp facility showed that the combinations of the boiling temperature ( $T_B$ ) prediction using NN with the  $p_{i,L}$   
501 empirical expressions using MY yielded the maximum  $C^*$  values while  $T_B$  by JB with  $p_{i,L}$  by NN yielded the minimum  $C^*$   
502 values (Figure S6 and S7). More details regarding the theoretical calculations are provided in the Supplement. The methods  
503 with the smallest and largest  $C^*$  values for the given compounds were chosen to represent the upper and lower limits of the  
504 possible theoretical values, when comparing to the observed ones. These limits are expressed in Figure 4 by the error bars on  
505 the x-axis with the marker points corresponding to their average. In total, 10 compounds were identified from previous  
506 publications to overlap with experimentally detected parent ions for the  $\beta$ -pinene ozonolysis experiment. For most of these  
507 compounds theoretical and experimental values agreed within the uncertainties. No significant discrepancies were found for

508 compounds in the SVOC volatility range. However, compounds in the IVOC range were underestimated from the  
509 experimental approaches when compared to theory. A characteristic IVOC 1<sup>st</sup> generation product from the  $\beta$ -pinene  
510 ozonolysis is nopinone that has been previously experimentally studied with a focus on the gas-to-particle partitioning  
511 (Steitz, 2010;Kahnt, 2012;Hohaus et al., 2015). Comparison of this work to previous studies was performed as it can be seen  
512 in Figure 4(a). The results showed agreement of the  $C^*$  within  $\pm 10^{0.5}$  between the experimental approaches while the theory  
513 showed differences of  $10^3$  in the  $C^*$  estimation. This comparison was extended to oxonopinone, being the second  
514 underestimated IVOC 1<sup>st</sup> generation product, where again this study ( $\log(C^*) = 3.16 \pm 0.13$ ) was in good agreement to  
515 Hohaus et al. (2015) ( $\log(C^*) = 3.16 \pm 0.12$ ) using GC-MS but the same sampling technique.

516 To better understand the differences of the experimental to the theoretical approaches, focus was given on the potential  
517 sources of uncertainties within both calculations. For the theoretical approach, the more complex the molecules with  
518 increasing functional groups were, the higher the uncertainty of the saturation vapor pressure and thus the volatility was.  
519 This is depicted by the higher error bars when moving towards SVOCs. First generation products like nopinone are not  
520 characterized by high complexity, thus theory provided more reliable thermodynamic values also reflected by the good  
521 agreement between all theoretical approaches (Figure S6 and S7). The experimental calculation of the volatility performed  
522 by the PTR-based techniques could be affected by the (i) existence of isomers within a studied  $m/z$  with different structural  
523 information and thus thermodynamic properties, (ii) thermal and ionic fragmentation of higher molecular weight compounds,  
524 produced by accretion and oligomerization reactions, down to the  $m/z$  detected by the instruments, (iii) phase-state of the  
525 bulk OA influencing the partitioning equilibrium time-scales ( $\tau_{eq}$ ) of the individual compounds.

526 Mass spectrometric measurement approaches provide by definition molecular formulas; however, a given formula does not  
527 correspond to an individual compound. Isaacman-VanWertz et al. (2017) showed that during the  $\alpha$ -pinene OH oxidation  
528 molecules with larger carbon atom numbers (C8 to C10) corresponded to an increased number of unique isomers for each  
529 molecular formula. Differences in the functionality of these isomers may be critical for studies of their thermodynamic  
530 properties. To reduce biases in this work, the different isomers seen from previous publications were included in the  
531 theoretical calculations. For the  $\beta$ -pinene experiment the isomers showed theoretical  $C^*$  values within the estimated  
532 uncertainty thus biasing to a minor extent this comparison. For formulas that corresponded to an individual compound like  
533 e.g. nopinone and oxonopinone further comparison to previous publications was performed. The experimentally calculated  
534  $C^*$  was in good agreement with previous studies using a GC-MS to detect particle-phase nopinone (Kahnt, 2012;Hohaus et  
535 al., 2015). Since GC-MS techniques are capable of providing the exact molecular structure of nopinone this further  
536 supported the identification of  $(C_9H_{14}O_1)H^+$  and  $(C_9H_{12}O_2)H^+$  as protonated nopinone and oxonopinone, respectively, in this  
537 study.

538 The treatment of the PTR dataset to exclude ions affected by thermal and ionic dissociation was described in detail in  
539 section 3.1. However, higher MW species (e.g. accretion reaction products or oligomers), of low volatility, which are not in  
540 the detection range of the PTR-ToF-MS, could decompose to lower MW species during thermal breakdown (Barsanti et al.,  
541 2017) (Tillmann et al., 2010). These species could be identified as a parent ion when using the parent ion identification  
542 method (section 3.1) consequently inducing an overestimation of their particulate phase concentrations. This effect is not  
543 constrained in the used method and could potentially and selectively decrease the volatility of certain species. To explain the  
544 differences in the  $C^*$  experimental vs theoretical estimations for nopinone, the ratio  $\frac{G_i}{P_i}$  from equation 2 should change by a  
545 factor of  $\sim 300$ . This would suggest a particulate-phase mass concentration 300 times lower than the observed one, in order  
546 to reach an agreement with the theoretical calculations. This fragmentation pathway should not only strongly affect the PTR-  
547 based techniques but also the previously mentioned GC-MS systems. The decomposition pathway would be narrowed to  
548 thermal dissociation during desorption, which is the only common pathway from all techniques. Finally, this thermal  
549 dissociation pathway needs to result in products with the exact chemical structure of nopinone.

550 When describing SOA formation, it is generally assumed that oxidation products rapidly adopt gas-to-particle equilibrium  
551 with the assumption of a homogeneously mixed condensed phase (Pankow, 1994; Odum et al., 1996). The non-ideal behavior  
552 of a complex organic mixture could introduce mixing effects, changing the activity coefficients of the individual organic  
553 molecules and thus their gas-to-particle equilibrium. Isotopic labeling experiments have confirmed that SOA derived from  
554 different precursors will interact in a relatively ideal fashion, thus introducing minor deviations of the activity coefficient  
555 from unity (Dommen et al., 2009; Hildebrandt et al., 2011). Furthermore, Hohaus et al. (2015) showed that for the  $\beta$ -pinene  
556 ozonolysis oxidation products the theoretically estimated activity coefficient values calculated by the thermodynamic group-  
557 contribution model AIOMFAC (Zuend et al., 2011) were far from explaining the differences between theory and  
558 observations. These findings further suggest that in this work, gas-to-particle partitioning was not strongly affected by  
559 activity coefficient deviations and thus could not explain the obtained differences. On the contrary, the phase-state of the  
560 bulk OA strongly affects the partitioning equilibrium time-scales ( $\tau_{\text{eq}}$ ) ranging from seconds in case of liquid particles to  
561 hours or days for semi-solid or glassy particles (Shiraiwa et al., 2011; Shiraiwa and Seinfeld, 2012). Biogenic SOA particles  
562 have been found to adopt an amorphous solid-, most probably glassy-state (Virtanen et al., 2010). The experimental  
563 conditions in this study (on average 55 % RH) suggest that a significant portion of the SOA can be in a semi-solid or glassy  
564 state (Bateman et al., 2015). This amorphous (semi-)solid-state may influence the partitioning of semi-volatile compounds,  
565 hindering the lower volatile species to leave the particles. Biogenic OA produced in this study would be thus directly  
566 affected by high partitioning equilibrium time-scales leading to increased particulate-phase concentrations of more volatile  
567 compounds “trapped” within this glassy-state of the OA. This would imply a direct decay of their volatility thus explaining  
568 the observed lower  $C^*$  values of the 1<sup>st</sup> generation products.

569 A comparison of the observed and calculated  $C^*$  was performed for all experiments during this campaign as shown in Figure  
570 5. There were 11, 12 and 9 compounds observed in the limonene, terpene and trees oxidation experiments, respectively,  
571 which were described in previous publications. These compounds can be attributed to only 5, 8 and 4 different molecular  
572 formulae ( $m/z$ ) suggesting an increased number of isomers found within these overlaps. The analysis yielded similar  
573 findings to those from the  $\beta$ -pinene experiment. The comparison between observations and theory showed relatively good  
574 agreement within the SVOC range for most of the compounds, while the  $C^*$  for compounds expected to be in the IVOC  
575 range was experimentally underestimated, i.e. the measured particle-phase concentrations were higher than those explained  
576 by the equilibrium partitioning theory. When moving from single to multiple precursor experiments e.g. from the ozonolysis  
577 of  $\beta$ -pinene to the ozonolysis and  $\text{NO}_3$  oxidation of limonene, the number of isomers increased rapidly, due to the higher  
578 complexity of the investigated systems. Certain isomers showed variations up to two orders of magnitude in their estimated  
579 volatility values. On the other hand, due to increased complexity of the systems, the limitations of the mass spectrometric  
580 techniques to define the molecular structure of the compounds might introduce large biases. However, despite these  
581 uncertainties, the theoretical volatility values were still found to be in fair agreement with the observations for all systems  
582 studied, suggesting that these deviations would still be within the already existing high uncertainties associated to the  
583 theoretical calculations.

584 There are two major effects that could be emphasized by presenting two case scenarios. In the first scenario the equilibrium  
585 partitioning theory correctly represents the studied systems. The experimental underestimation of the IVOCs (and certain  
586 SVOCs) volatility can thus only be explained by experimental uncertainties due to (i) fragmentation of higher MW  
587 compounds and oligomers to the detection range of the PTR-based techniques, and/or (ii) the existence of isomers with high  
588 volatility differences. However as mentioned before, studies which performed molecular identification of compounds (e.g.  
589 nopinone) show significantly different experimentally derived partitioning coefficient values when compared to theoretical  
590 calculations (Hohaus et al., 2015; Kahnt et al., 2012), therefore isomers could not explain this discrepancy for all cases. In  
591 the second scenario the assumption of equilibrium partitioning would be questioned due to the findings that BSOA form a  
592 glassy phase-state and thus gas-to-particle equilibrium might not be reached. This would imply that all theoretical

593 calculations performed in this study and used in models to describe SOA formation would be developed under the wrong  
594 assumption, thus decreasing their reliability. This work provides clear evidence pointing towards these two effects but cannot  
595 provide a quantitative estimate to their individual contribution. Future studies combining the information provided by the  
596 PTR-based techniques with SOA phase-state measurements are essential. In order to bridge the gap between experimental  
597 data and theoretical volatility calculations further development of instrumentation providing structural information at a  
598 molecular level is required. Techniques like the TAG (Williams et al., 2006; Isaacman et al., 2014; Zhang et al., 2014)  
599 coupled in parallel to the PTR-based techniques could provide further insight into different isomeric structures.  
600

#### 601 4 Summary

602 We have presented the first laboratory inter-comparison of three in-situ, near real-time measurement techniques of gas-to-  
603 particle partitioning with a focus on biogenic SOA formation and oxidation. These thermal desorption techniques are known  
604 to be affected by thermal dissociation during desorption and ionic dissociation during ionization in the drift tube of the  
605 PTRMS (Gkatzelis et al., 2018). These fragmentation pathways could directly affect the gas-to-particle partitioning and thus  
606 the saturation mass concentration ( $C^*$ ) calculation. To reduce fragmentation biases a method to identify and exclude ions  
607 affected by these decomposition pathways was developed and applied. Narrow volatility distributions were observed ranging  
608 from 0 to 4 with species in the semi-volatile (SVOCs) to intermediate volatility (IVOCs) regime. The limonene oxidation  
609 experiment showed a lower volatility distribution when compared to the  $\beta$ -pinene oxidation experiment further supporting  
610 that limonene SOA are less volatile than  $\beta$ -pinene SOA (Lee et al., 2011). When comparing  $C^*$  values obtained for species  
611 observed from all techniques, instruments showed good agreement within 1 decade, with deviations explained by the  
612 different operating conditions of the PTRMS (Gkatzelis et al., 2018).

613 Determined species were mapped onto the 2D-VBS framework and results showed a decrease of the  $C^*$  with increasing  
614 oxidation state and increasing oxygen atom number in accordance to previous findings (Jimenez et al., 2009; Kroll, 2011).  
615 These species accounted for 20-30 % of the total organic mass measured from an AMS. For species that overlapped with  
616 compounds from previous publications a comparison to theoretical calculations was performed based on their molecular  
617 structure. Accounting for the uncertainties of the measurements, results showed good agreement for SVOCs, while IVOCs  
618 introduced higher deviations. Detailed comparison of the partitioning values of nopinone, a 1<sup>st</sup> generation product from the  
619 ozonolysis of  $\beta$ -pinene, was performed to previous publications. Results showed agreement of the  $C^*$  within  $\pm 10^{0.5}$  between  
620 all experimental approaches while theory showed differences of  $10^3$  on the  $C^*$  estimation. These major differences are  
621 discussed in terms of possible uncertainties biasing the experimental values from (1) existence of isomers within a studied  
622  $m/z$ , (2) thermal and ionic fragmentation of higher molecular weight compounds, produced by accretion and oligomerization  
623 reactions, fragmenting to  $m/z$ 's detected by the instruments, (3) Non-idealities of the organic mixtures and (4) the phase-state  
624 of the bulk OA affecting the partitioning equilibrium time-scales ( $\tau_{eq}$ ) of the individual compounds. Results point towards  
625 possible interferences by thermal and ionic fragmentation as well as kinetic influences in the distribution between gas- and  
626 particle-phase with diffusivity in the particle-phase and irreversible uptake. These findings further promote future work and  
627 parallel measurement of the phase-state of the OA combined with compound specific volatility determination from the PTR-  
628 based techniques.  
629

630 **5 References**

- 631 An, W. J., Pathak, R. K., Lee, B.-H., and Pandis, S. N.: Aerosol volatility measurement using an improved thermodenuder:  
632 Application to secondary organic aerosol, *J Aerosol Sci*, 38, 305-314, 10.1016/j.jaerosci.2006.12.002, 2007.
- 633
- 634 Barsanti, K. C., Kroll, J. H., and Thornton, J. A.: Formation of low-volatility organic compounds in the atmosphere: Recent  
635 advancements and insights, *J Phys Chem Lett*, 8, 1503-1511, 10.1021/acs.jpcclett.6b02969, 2017.
- 636
- 637 Bateman, A. P., Gong, Z., Liu, P., Sato, B., Cirino, G., Zhang, Y., Artaxo, P., Bertram, A. K., Manzi, A. O., Rizzo, L. V.,  
638 Souza, R. A. F., Zaveri, R. A., and Martin, S. T.: Sub-micrometre particulate matter is primarily in liquid form over amazon  
639 rainforest, *Nat Geosci*, 9, 34, 10.1038/ngeo2599, 2015.
- 640
- 641 Bilde, M., Barsanti, K., Booth, M., Cappa, C. D., Donahue, N. M., Emanuelsson, E. U., McFiggans, G., Krieger, U. K.,  
642 Marcolli, C., Topping, D., Ziemann, P., Barley, M., Clegg, S., Dennis-Smith, B., Hallquist, M., Hallquist, A. M., Khlystov,  
643 A., Kulmala, M., Mogensen, D., Percival, C. J., Pope, F., Reid, J. P., Ribeiro da Silva, M. A., Rosenoern, T., Salo, K.,  
644 Soonsin, V. P., Yli-Juuti, T., Prisle, N. L., Pagels, J., Rarey, J., Zardini, A. A., and Riipinen, I.: Saturation vapor pressures  
645 and transition enthalpies of low-volatility organic molecules of atmospheric relevance: From dicarboxylic acids to complex  
646 mixtures, *Chem Rev*, 115, 4115-4156, 10.1021/cr5005502, 2015.
- 647
- 648 Booth, A. M., Markus, T., McFiggans, G., Percival, C. J., McGillen, M. R., and Topping, D. O.: Design and construction of  
649 a simple knudsen effusion mass spectrometer (kems) system for vapour pressure measurements of low volatility organics,  
650 *Atmos Meas Tech*, 2, 355-361, 10.5194/amt-2-355-2009, 2009.
- 651
- 652 Camredon, M., Hamilton, J. F., Alam, M. S., Wyche, K. P., Carr, T., White, I. R., Monks, P. S., Rickard, A. R., and Bloss,  
653 W. J.: Distribution of gaseous and particulate organic composition during dark  $\alpha$ -pinene ozonolysis, *Atmos Chem Phys*, 10,  
654 2893-2917, 2010.
- 655
- 656 Canagaratna, M. R., Jayne, J. T., Jimenez, J. L., Allan, J. D., Alfarra, M. R., Zhang, Q., Onasch, T. B., Drewnick, F., Coe,  
657 H., Middlebrook, A., Delia, A., Williams, L. R., Trimborn, A. M., Northway, M. J., DeCarlo, P. F., Kolb, C. E., Davidovits,  
658 P., and Worsnop, D. R.: Chemical and microphysical characterization of ambient aerosols with the aerodyne aerosol mass  
659 spectrometer, *Mass Spectrom Rev*, 26, 185-222, 10.1002/mas.20115, 2007.
- 660
- 661 Canagaratna, M. R., Jimenez, J. L., Kroll, J. H., Chen, Q., Kessler, S. H., Massoli, P., Hildebrandt Ruiz, L., Fortner, E.,  
662 Williams, L. R., Wilson, K. R., Surratt, J. D., Donahue, N. M., Jayne, J. T., and Worsnop, D. R.: Elemental ratio  
663 measurements of organic compounds using aerosol mass spectrometry: Characterization, improved calibration, and  
664 implications, *Atmos Chem Phys*, 15, 253-272, 10.5194/acp-15-253-2015, 2015.
- 665
- 666 Cappa, C. D., and Jimenez, J. L.: Quantitative estimates of the volatility of ambient organic aerosol, *Atmos Chem Phys*, 10,  
667 5409-5424, 10.5194/acp-10-5409-2010, 2010.
- 668
- 669 Chen, J., and Griffin, R.: Modeling secondary organic aerosol formation from oxidation of -pinene, -pinene, and -limonene,  
670 *Atmospheric Environment*, 39, 7731-7744, 10.1016/j.atmosenv.2005.05.049, 2005.
- 671
- 672 Clegg, S. L., Seinfeld, J. H., and Brimblecombe, P.: Thermodynamic modelling of aqueous aerosols containing electrolytes  
673 and dissolved organic compounds, *J Aerosol Sci*, 32, 713-738, 2001.
- 674
- 675 Compernelle, S., Ceulemans, K., and Müller, J. F.: Technical note: Vapor pressure estimation methods applied to secondary  
676 organic aerosol constituents from  $\alpha$ -pinene oxidation: An intercomparison study, *Atmos Chem Phys*, 10, 6271-6282,  
677 10.5194/acp-10-6271-2010, 2010.
- 678
- 679 Daumit, K. E., Kessler, S. H., and Kroll, J. H.: Average chemical properties and potential formation pathways of highly  
680 oxidized organic aerosol, *Faraday Discussions*, 165, 181-202, 10.1039/C3FD00045A, 2013.
- 681
- 682 de Gouw, J. A., Brock, C. A., Atlas, E. L., Bates, T. S., Fehsenfeld, F. C., Goldan, P. D., Holloway, J. S., Kuster, W. C.,  
683 Lerner, B. M., Matthew, B. M., Middlebrook, A. M., Onasch, T. B., Peltier, R. E., Quinn, P. K., Senff, C. J., Stohl, A.,  
684 Sullivan, A. P., Trainer, M., Warneke, C., Weber, R. J., and Williams, E. J.: Sources of particulate matter in the northeastern  
685 united states in summer: 1. Direct emissions and secondary formation of organic matter in urban plumes, *J Geophys Res*,  
686 113, 10.1029/2007jd009243, 2008.
- 687
- 688 DeCarlo, P. F., Kimmel, J. R., Trimborn, A., Northway, M. J., Jayne, J. T., Aiken, A. C., Gonin, M., Fuhrer, K., Horvath, T.,  
689 Docherty, K. S., Worsnop, D. R., and Jimenez, J. L.: Field-deployable, high-resolution, time-of-flight aerosol mass  
690 spectrometer, *Anal Chem*, 78, 8281-8289, 10.1021/ac061249n, 2006.
- 691



692 Dommen, J., Hellén, H., Saurer, M., Jaeggi, M., Siegwolf, R., Metzger, A., Duplissy, J., Fierz, M., and Baltensperger, U.:  
693 Determination of the aerosol yield of isoprene in the presence of an organic seed with carbon isotope analysis, *Environ Sci*  
694 *Technol*, 43, 6697-6702, 10.1021/es9006959, 2009.

695

696 Donahue, N. M., Robinson, A. L., Stanier, C. O., and Pandis, S. N.: Coupled partitioning, dilution, and chemical aging of  
697 semivolatile organics, *Environ Sci Technol*, 40, 2635-2643, 10.1021/es052297c, 2006.

698

699 Donahue, N. M., Epstein, S. A., Pandis, S. N., and Robinson, A. L.: A two-dimensional volatility basis set: 1. Organic-  
700 aerosol mixing thermodynamics, *Atmos Chem Phys*, 11, 3303-3318, 10.5194/acp-11-3303-2011, 2011.

701

702 Donahue, N. M., Kroll, J. H., Pandis, S. N., and Robinson, A. L.: A two-dimensional volatility basis set – part 2: Diagnostics  
703 of organic-aerosol evolution, *Atmos Chem Phys*, 12, 615-634, 10.5194/acp-12-615-2012, 2012.

704

705 Donahue, N. M., Chuang, W., Epstein, S. A., Kroll, J. H., Worsnop, D. R., Robinson, A. L., Adams, P. J., and Pandis, S. N.:  
706 Why do organic aerosols exist? Understanding aerosol lifetimes using the two-dimensional volatility basis set, *Environ*  
707 *Chem*, 10, 151, 10.1071/en13022, 2013.

708

709 Donahue, N. M., Robinson, A. L., Trump, E. R., Riipinen, I., and Kroll, J. H.: Volatility and aging of atmospheric organic  
710 aerosol, *Top Curr Chem*, 339, 97-143, 10.1007/128\_2012\_355, 2014.

711

712 Duncianu, M., David, M., Kartigeyane, S., Cirtog, M., Doussin, J. F., and Picquet-Varrault, B.: Measurement of alkyl and  
713 multifunctional organic nitrates by proton-transfer-reaction mass spectrometry, *Atmos Meas Tech*, 10, 1445-1463,  
714 10.5194/amt-10-1445-2017, 2017.

715

716 Ehn, M., Thornton, J. A., Kleist, E., Sipila, M., Junninen, H., Pullinen, I., Springer, M., Rubach, F., Tillmann, R., Lee, B.,  
717 Lopez-Hilfiker, F., Andres, S., Acir, I. H., Rissanen, M., Jokinen, T., Schobesberger, S., Kangasluoma, J., Kontkanen, J.,  
718 Nieminen, T., Kurten, T., Nielsen, L. B., Jorgensen, S., Kjaergaard, H. G., Canagaratna, M., Maso, M. D., Berndt, T., Petaja,  
719 T., Wahner, A., Kerminen, V. M., Kulmala, M., Worsnop, D. R., Wildt, J., and Mentel, T. F.: A large source of low-  
720 volatility secondary organic aerosol, *Nature*, 506, 476-479, 10.1038/nature13032, 2014.

721

722 Eichler, P., Muller, M., D'Anna, B., and Wisthaler, A.: A novel inlet system for online chemical analysis of semi-volatile  
723 submicron particulate matter, *Atmos Meas Tech*, 8, 1353-1360, DOI 10.5194/amt-8-1353-2015, 2015.

724

725 Eichler, P., Müller, M., Rohmann, C., Stengel, B., Orasche, J., Zimmermann, R., and Wisthaler, A.: Lubricating oil as a  
726 major constituent of ship exhaust particles, *Environ Sci Tech Let*, 4, 54-58, 10.1021/acs.estlett.6b00488, 2017.

727

728 Epstein, S. A., Riipinen, I., and Donahue, N. M.: A semiempirical correlation between enthalpy of vaporization and  
729 saturation concentration for organic aerosol, *Environ Sci Technol*, 44, 743-748, 10.1021/es902497z, 2010.

730

731 Faulhaber, A. E., Thomas, B. M., Jimenez, J. L., Jayne, J. T., Worsnop, D. R., and Ziemann, P. J.: Characterization of a  
732 thermodenuder-particle beam mass spectrometer system for the study of organic aerosol volatility and composition, *Atmos*  
733 *Meas Tech*, 2, 15-31, 10.5194/amt-2-15-2009, 2009.

734

735 Fredenslund, A., Jones, R. L., and Prausnitz, J. M.: Group-contribution estimation of activity coefficients in nonideal liquid  
736 mixtures, *AIChE J*, 21, 1086-1099, 1975.

737

738 Gkatzelis, G. I., Papanastasiou, D. K., Florou, K., Kaltsonoudis, C., Louvaris, E., and Pandis, S. N.: Measurement of  
739 nonvolatile particle number size distribution, *Atmos Meas Tech*, 9, 103-114, 10.5194/amt-9-103-2016, 2016.

740

741 Gkatzelis, G. I., Tillmann, R., Hohaus, T., Müller, M., Eichler, P., Xu, K. M., Schlag, P., Schmitt, S. H., Wegener, R.,  
742 Kaminski, M., Holzinger, R., Wisthaler, A., and Kiendler-Scharr, A.: Comparison of three aerosol chemical characterization  
743 techniques utilizing ptr-tof-ms: A study on freshly formed and aged biogenic soa, *Atmos. Meas. Tech.*, 11, 1481-1500,  
744 10.5194/amt-11-1481-2018, 2018.

745

746 Goldstein, A. H., Worton, D. R., Williams, B. J., Hering, S. V., Kreisberg, N. M., Panić, O., and Górecki, T.: Thermal  
747 desorption comprehensive two-dimensional gas chromatography for in-situ measurements of organic aerosols, *J Chromatogr*  
748 *A*, 1186, 340-347, <https://doi.org/10.1016/j.chroma.2007.09.094>, 2008.

749

750 Hallquist, M., Wenger, J. C., Baltensperger, U., Rudich, Y., Simpson, D., Claeys, M., Dommen, J., Donahue, N. M., George,  
751 C., Goldstein, A. H., Hamilton, J. F., Herrmann, H., Hoffmann, T., Iinuma, Y., Jang, M., Jenkin, M. E., Jimenez, J. L.,  
752 Kiendler-Scharr, A., Maenhaut, W., McFiggans, G., Mentel, T. F., Monod, A., Prévôt, A. S. H., Seinfeld, J. H., Surratt, J. D.,  
753 Szmigielski, R., and Wildt, J.: The formation, properties and impact of secondary organic aerosol: Current and emerging  
754 issues, *Atmos Chem Phys*, 9, 5155-5236, 10.5194/acp-9-5155-2009, 2009.

755

756 Hildebrandt, L., Henry, K. M., Kroll, J. H., Worsnop, D. R., Pandis, S. N., and Donahue, N. M.: Evaluating the mixing of  
757 organic aerosol components using high-resolution aerosol mass spectrometry, *Environ Sci Technol*, 45, 6329-6335,  
758 10.1021/es200825g, 2011.

759

760 Hohaus, T., Trimborn, D., Kiendler-Scharr, A., Gensch, I., Laumer, W., Kammer, B., Andres, S., Boudries, H., Smith, K. A.,  
761 Worsnop, D. R., and Jayne, J. T.: A new aerosol collector for quasi on-line analysis of particulate organic matter: The  
762 aerosol collection module (acm) and first applications with a gc/ms-fid, *Atmos Meas Tech*, 3, 1423-1436, DOI 10.5194/amt-  
763 3-1423-2010, 2010.

764

765 Hohaus, T., Gensch, I., Kimmel, J. R., Worsnop, D. R., and Kiendler-Scharr, A.: Experimental determination of the  
766 partitioning coefficient of  $\beta$ -pinene oxidation products in soas, *Physical Chemistry Chemical Physics*, 17, 14796-14804,  
767 10.1039/C5CP01608H, 2015.

768

769 Hohaus, T., Kuhn, U., Andres, S., Kaminski, M., Rohrer, F., Tillmann, R., Wahner, A., Wegener, R., Yu, Z., and Kiendler-  
770 Scharr, A.: A new plant chamber facility, plus, coupled to the atmosphere simulation chamber saphir, *Atmos Meas Tech*, 9,  
771 1247-1259, 10.5194/amt-9-1247-2016, 2016.

772

773 Holzinger, R., Williams, J., Herrmann, F., Lelieveld, J., Donahue, N. M., and Rockmann, T.: Aerosol analysis using a  
774 thermal-desorption proton-transfer-reaction mass spectrometer (td-ptr-ms): A new approach to study processing of organic  
775 aerosols, *Atmos Chem Phys*, 10, 2257-2267, 2010.

776

777 Huffman, J. A., Ziemann, P. J., Jayne, J. T., Worsnop, D. R., and Jimenez, J. L.: Development and characterization of a fast-  
778 stepping/scanning thermodenuder for chemically-resolved aerosol volatility measurements, *Aerosol Sci Tech*, 42, 395-407,  
779 10.1080/02786820802104981, 2008.

780

781 Isaacman-VanWertz, G., Yee, L. D., Kreisberg, N. M., Wernis, R., Moss, J. A., Hering, S. V., de Sa, S. S., Martin, S. T.,  
782 Alexander, M. L., Palm, B. B., Hu, W., Campuzano-Jost, P., Day, D. A., Jimenez, J. L., Riva, M., Surratt, J. D., Viegas, J.,  
783 Manzi, A., Edgerton, E., Baumann, K., Souza, R., Artaxo, P., and Goldstein, A. H.: Ambient gas-particle partitioning of  
784 tracers for biogenic oxidation, *Environ Sci Technol*, 10.1021/acs.est.6b01674, 2016.

785

786 Isaacman-VanWertz, G., Massoli, P., O'Brien, R. E., Nowak, J. B., Canagaratna, M. R., Jayne, J. T., Worsnop, D. R., Su, L.,  
787 Knopf, D. A., Misztal, P. K., Arata, C., Goldstein, A. H., and Kroll, J. H.: Using advanced mass spectrometry techniques to  
788 fully characterize atmospheric organic carbon: Current capabilities and remaining gaps, *Faraday Discussions*,  
789 10.1039/C7FD00021A, 2017.

790

791 Isaacman, G., Kreisberg, N. M., Yee, L. D., Worton, D. R., Chan, A. W. H., Moss, J. A., Hering, S. V., and Goldstein, A. H.:  
792 Online derivatization for hourly measurements of gas- and particle-phase semi-volatile oxygenated organic compounds by  
793 thermal desorption aerosol gas chromatography (sv-tag), *Atmos Meas Tech*, 7, 4417-4429, DOI 10.5194/amt-7-4417-2014,  
794 2014.

795

796 Jang, M., and Kamens, R. M.: Atmospheric secondary aerosol formation by heterogeneous reactions of aldehydes in the  
797 presence of a sulfuric acid aerosol catalyst, *Environ Sci Technol*, 35, 4758-4766, 10.1021/es010790s, 2001.

798

799 Jaoui, M., Corse, E., Kleindienst, T. E., Offenberg, J. H., Lewandowski, M., and Edney, E. O.: Analysis of secondary  
800 organic aerosol compounds from the photooxidation of d-limonene in the presence of nox and their detection in ambient  
801 pm<sub>2.5</sub>, *Environmental Science & Technology*, 40, 3819-3828, 10.1021/es052566z, 2006.

802

803 Jenkin, M. E.: Modelling the formation and composition of secondary organic aerosol from  $\alpha$ - and  $\beta$ -pinene ozonolysis  
804 using mcm v3 *Atmospheric Chemistry and Physics*, 4, 1741-1757, 2004.

805

806 Jimenez, J. L., Canagaratna, M. R., Donahue, N. M., Prevot, A. S. H., Zhang, Q., Kroll, J. H., DeCarlo, P. F., Allan, J. D.,  
807 Coe, H., Ng, N. L., Aiken, A. C., Docherty, K. S., Ulbrich, I. M., Grieshop, A. P., Robinson, A. L., Duplissy, J., Smith, J. D.,  
808 Wilson, K. R., Lanz, V. A., Hueglin, C., Sun, Y. L., Tian, J., Laaksonen, A., Raatikainen, T., Rautiainen, J., Vaattovaara, P.,  
809 Ehn, M., Kulmala, M., Tomlinson, J. M., Collins, D. R., Cubison, M. J., Dunlea, J., Huffman, J. A., Onasch, T. B., Alfarra,  
810 M. R., Williams, P. I., Bower, K., Kondo, Y., Schneider, J., Drewnick, F., Borrmann, S., Weimer, S., Demerjian, K.,  
811 Salcedo, D., Cottrell, L., Griffin, R., Takami, A., Miyoshi, T., Hatakeyama, S., Shimono, A., Sun, J. Y., Zhang, Y. M.,  
812 Dzepina, K., Kimmel, J. R., Sueper, D., Jayne, J. T., Herndon, S. C., Trimborn, A. M., Williams, L. R., Wood, E. C.,  
813 Middlebrook, A. M., Kolb, C. E., Baltensperger, U., and Worsnop, D. R.: Evolution of organic aerosols in the atmosphere,  
814 *Science*, 326, 10.1126/science.1180353, 2009.

815

816 Joback, K. G., and Reid, R. C.: Estimation of pure-component properties from group contributions, *Chem Eng Commun*, 57,  
817 233-243, 10.1080/00986448708960487, 1987.

818

819 Kahnt, A.: Semivolatile compounds from atmospheric monoterpene oxidation PhD, Fakultät für Chemie und Mineralogie,  
820 Universität Leipzig, Leipzig, Germany, 205 pp., 2012.

821

822 Karnezi, E., Riipinen, I., and Pandis, S. N.: Measuring the atmospheric organic aerosol volatility distribution: A theoretical  
823 analysis, *Atmos Meas Tech*, 7, 2953-2965, 10.5194/amt-7-2953-2014, 2014.

824

825 Krechmer, J. E., Coggon, M. M., Massoli, P., Nguyen, T. B., Crounse, J. D., Hu, W., Day, D. A., Tyndall, G. S., Henze, D.  
826 K., Rivera-Rios, J. C., Nowak, J. B., Kimmel, J. R., Mauldin, R. L., 3rd, Stark, H., Jayne, J. T., Sipila, M., Junninen, H.,  
827 Clair, J. M., Zhang, X., Feiner, P. A., Zhang, L., Miller, D. O., Brune, W. H., Keutsch, F. N., Wennberg, P. O., Seinfeld, J.  
828 H., Worsnop, D. R., Jimenez, J. L., and Canagaratna, M. R.: Formation of low volatility organic compounds and secondary  
829 organic aerosol from isoprene hydroxyhydroperoxide low-no oxidation, *Environ Sci Technol*, 49, 10330-10339,  
830 10.1021/acs.est.5b02031, 2015.

831

832 Kreisberg, N. M., Hering, S. V., Williams, B. J., Worton, D. R., and Goldstein, A. H.: Quantification of hourly speciated  
833 organic compounds in atmospheric aerosols, measured by an in-situ thermal desorption aerosol gas chromatograph (tag),  
834 *Aerosol Sci Tech*, 43, 38-52, 10.1080/02786820802459583, 2009.

835

836 Kroll, J. H.: Carbon oxidation state as a metric for describing the chemistry of atmospheric organic aerosol, *Nat Chem*, 3,  
837 10.1038/nchem.948, 2011.

838

839 Kundu, S., Fisseha, R., Putman, A. L., Rahn, T. A., and Mazzoleni, L. R.: High molecular weight soa formation during  
840 limonene ozonolysis: Insights from ultrahigh-resolution ft-icr mass spectrometry characterization, *Atmospheric Chemistry  
841 and Physics*, 12, 5523-5536, 10.5194/acp-12-5523-2012, 2012.

842

843 Lee, B.-H., Pierce, J. R., Engelhart, G. J., and Pandis, S. N.: Volatility of secondary organic aerosol from the ozonolysis of  
844 monoterpenes, *Atmos Environ*, 45, 2443-2452, 10.1016/j.atmosenv.2011.02.004, 2011.

845

846 Leungsakul, S., Jaoui, M., and Kamens, R. M.: Kinetic mechanism for predicting secondary organic aerosol formation from  
847 the reaction of d-limonene with ozone, *Environmental Science & Technology*, 39, 9583-9594, 10.1021/es0492687, 2005a.

848

849 Leungsakul, S., Jeffries, H. E., and Kamens, R. M.: A kinetic mechanism for predicting secondary aerosol formation from  
850 the reactions of d-limonene in the presence of oxides of nitrogen and natural sunlight, *Atmospheric Environment*, 39, 7063-  
851 7082, 10.1016/j.atmosenv.2005.08.024, 2005b.

852

853 Li, Y., Pöschl, U., and Shiraiwa, M.: Molecular corridors and parameterizations of volatility in the chemical evolution of  
854 organic aerosols, *Atmos. Chem. Phys.*, 16, 3327-3344, 10.5194/acp-16-3327-2016, 2016.

855

856 Lopez-Hilfiker, F. D., Mohr, C., Ehn, M., Rubach, F., Kleist, E., Wildt, J., Mentel, T. F., Lutz, A., Hallquist, M., Worsnop,  
857 D., and Thornton, J. A.: A novel method for online analysis of gas and particle composition: Description and evaluation of a  
858 filter inlet for gases and aerosols (figaero), *Atmos Meas Tech*, 7, 983-1001, DOI 10.5194/amt-7-983-2014, 2014.

859

860 Lopez-Hilfiker, F. D., Mohr, C., Ehn, M., Rubach, F., Kleist, E., Wildt, J., Mentel, T. F., Carrasquillo, A. J., Daumit, K. E.,  
861 Hunter, J. F., Kroll, J. H., Worsnop, D. R., and Thornton, J. A.: Phase partitioning and volatility of secondary organic aerosol  
862 components formed from  $\alpha$ -pinene ozonolysis and oh oxidation: The importance of accretion products and other low  
863 volatility compounds, *Atmos Chem Phys*, 15, 7765-7776, 10.5194/acp-15-7765-2015, 2015.

864

865 Lopez-Hilfiker, F. D., Mohr, C., D'Ambro, E. L., Lutz, A., Riedel, T. P., Gaston, C. J., Iyer, S., Zhang, Z., Gold, A., Surratt,  
866 J. D., Lee, B. H., Kurten, T., Hu, W. W., Jimenez, J., Hallquist, M., and Thornton, J. A.: Molecular composition and  
867 volatility of organic aerosol in the southeastern u.S.: Implications for iepox derived soa, *Environ Sci Technol*, 50, 2200-  
868 2209, 10.1021/acs.est.5b04769, 2016.

869

870 Louvaris, E. E., Florou, K., Karnezi, E., Papanastasiou, D. K., Gkatzelis, G. I., and Pandis, S. N.: Volatility of source  
871 apportioned wintertime organic aerosol in the city of athens, *Atmos Environ*, 158, 138-147,  
872 10.1016/j.atmosenv.2017.03.042, 2017.

873

874 Mackay, D., Bobra, A., Chan, D. W., and Shiu, W. Y.: Vapor-pressure correlations for low-volatility environmental  
875 chemicals, *Environ Sci Technol*, 16, 645-649, 10.1021/es00104a004, 1982.

876

877 Martinez, R. E., Williams, B. J., Zhang, Y., Hagan, D., Walker, M., Kreisberg, N. M., Hering, S. V., Hohaus, T., Jayne, J. T.,  
878 and Worsnop, D. R.: Development of a volatility and polarity separator (vaps) for volatility- and polarity-resolved organic  
879 aerosol measurement, *Aerosol Sci Tech*, 50, 255-271, 10.1080/02786826.2016.1147645, 2016.

880

881 McFiggans, G., Topping, D. O., and Barley, M. H.: The sensitivity of secondary organic aerosol component partitioning to  
882 the predictions of component properties – part 1: A systematic evaluation of some available estimation techniques, *Atmos*  
883 *Chem Phys*, 10, 10255-10272, 10.5194/acp-10-10255-2010, 2010.

884

885 Mitchem, L., and Reid, J. P.: Optical manipulation and characterisation of aerosol particles using a single-beam gradient  
886 force optical trap, *Chem Soc Rev*, 37, 756-769, 10.1039/b609713h, 2008.

887

888 Murphy, B. N., Donahue, N. M., Fountoukis, C., Dall'Osto, M., O'Dowd, C., Kiendler-Scharr, A., and Pandis, S. N.:  
889 Functionalization and fragmentation during ambient organic aerosol aging: Application of the 2-d volatility basis set to field  
890 studies, *Atmos Chem Phys*, 12, 10797-10816, 10.5194/acp-12-10797-2012, 2012.

891

892 Myrdal, P. B., and Yalkowsky, S. H.: Estimating pure component vapor pressures of complex organic molecules, *Ind Eng*  
893 *Chem Res*, 36, 2494-2499, 10.1021/ie950242l, 1997.

894

895 Nannoolal, Y., Rarey, J., and Ramjugernath, D.: Estimation of pure component properties. Part 3. Estimation of the vapor  
896 pressure of non-electrolyte organic compounds via group contributions and group interaction, *Fluid Phase Equilib*, 269, 117-  
897 133, 10.1016/j.fluid.2008.04.020, 2008.

898

899 Odum, J. R., Hoffmann, T., Bowman, F., Collins, D., Flagan, R. C., and Seinfeld, J. H.: Gas/particle partitioning and  
900 secondary organic aerosol yields, *Environ Sci Technol*, 30, 2580-2585, 10.1021/es950943+, 1996.

901

902 Pankow, J. F.: An absorption model of gas/particle partitioning of organic compounds in the atmosphere, *Atmos Environ*,  
903 28, 185-188, 1994.

904

905 Pankow, J. F., and Asher, W. E.: Simpol.1: A simple group contribution method for predicting vapor pressures and  
906 enthalpies of vaporization of multifunctional organic compounds, *Atmos Chem Phys*, 8, 2773-2796, 10.5194/acp-8-2773-  
907 2008, 2008.

908

909 Pankow, J. F., and Barsanti, K. C.: The carbon number-polarity grid: A means to manage the complexity of the mix of  
910 organic compounds when modeling atmospheric organic particulate matter, *Atmos Environ*, 43, 2829-2835,  
911 10.1016/j.atmosenv.2008.12.050, 2009.

912

913 Pope, F. D., Dennis-Smith, B. J., Griffiths, P. T., Clegg, S. L., and Cox, R. A.: Studies of single aerosol particles  
914 containing malonic acid, glutaric acid, and their mixtures with sodium chloride. I. Hygroscopic growth, *J Phys Chem-US*,  
915 114, 5335-5341, 2010.

916

917 Praplan, A. P., Schobesberger, S., Bianchi, F., Rissanen, M. P., Ehn, M., Jokinen, T., Junninen, H., Adamov, A., Amorim,  
918 A., Dommen, J., Duplissy, J., Hakala, J., Hansel, A., Heinritzi, M., Kangasluoma, J., Kirkby, J., Krapf, M., Kürten, A.,  
919 Lehtipalo, K., Riccobono, F., Rondo, L., Sarnela, N., Simon, M., Tomé, A., Tröstl, J., Winkler, P. M., Williamson, C., Ye,  
920 P., Curtius, J., Baltensperger, U., Donahue, N. M., Kulmala, M., and Worsnop, D. R.: Elemental composition and clustering  
921 of  $\alpha$ -pinene oxidation products for different oxidation conditions, *Atmospheric Chemistry and Physics Discussions*, 14,  
922 30799-30833, 10.5194/acpd-14-30799-2014, 2014.

923

924 Prisle, N. L., Engelhart, G. J., Bilde, M., and Donahue, N. M.: Humidity influence on gas-particle phase partitioning of  $\alpha$ -  
925 pinene + o3secondary organic aerosol, *Geophys Res Lett*, 37, n/a-n/a, 10.1029/2009gl041402, 2010.

926

927 Riipinen, I., Pierce, J. R., Donahue, N. M., and Pandis, S. N.: Equilibration time scales of organic aerosol inside  
928 thermodenuders: Evaporation kinetics versus thermodynamics, *Atmos Environ*, 44, 597-607,  
929 10.1016/j.atmosenv.2009.11.022, 2010.

930

931 Rohrer, F., Bohn, B., Brauers, T., Brüning, D., Johnen, F. J., Wahner, A., and Kleffmann, J.: Characterisation of the  
932 photolytic hono-source in the atmosphere simulation chamber saphir, *Atmos Chem Phys*, 5, 2189-2201, 10.5194/acp-5-  
933 2189-2005, 2005.

934

935 Shiraiwa, M., Ammann, M., Koop, T., and Pöschl, U.: Gas uptake and chemical aging of semisolid organic aerosol particles,  
936 *PNAS*, 108, 11003-11008, 10.1073/pnas.1103045108, 2011.

937

938 Shiraiwa, M., and Seinfeld, J. H.: Equilibration timescale of atmospheric secondary organic aerosol partitioning, *Geophys*  
939 *Res Lett*, 39, n/a-n/a, 10.1029/2012gl054008, 2012.

940

941 Stark, H., Yatavelli, R. L. N., Thompson, S. L., Kang, H., Krechmer, J. E., Kimmel, J. R., Palm, B. B., Hu, W., Hayes, P. L.,  
942 Day, D. A., Campuzano-Jost, P., Canagaratna, M. R., Jayne, J. T., Worsnop, D. R., and Jimenez, J. L.: Impact of thermal  
943 decomposition on thermal desorption instruments: Advantage of thermogram analysis for quantifying volatility distributions  
944 of organic species, *Environ Sci Technol*, 10.1021/acs.est.7b00160, 2017.

945  
946 Stein, S. E., and Brown, R. L.: Estimation of normal boiling points from group contributions, *J Chem Inf Comp Sci*, 34, 581-  
947 587, 1994.  
948  
949 Steitz, B.: Experimental determination of the partitioning coefficient of nopinone as a marker substance in organic aerosol,  
950 PhD, Institute of Energy and Climate: Troposphere (IEK-8), Wuppertal University, Forschungszentrum Jülich GmbH, 2010.  
951  
952 Thompson, S. L., Yatavelli, R. L. N., Stark, H., Kimmel, J. R., Krechmer, J. E., Day, D. A., Hu, W., Isaacman-VanWertz,  
953 G., Yee, L., Goldstein, A. H., Khan, M. A. H., Holzinger, R., Kreisberg, N., Lopez-Hilfiker, F. D., Mohr, C., Thornton, J. A.,  
954 Jayne, J. T., Canagaratna, M., Worsnop, D. R., and Jimenez, J. L.: Field intercomparison of the gas/particle partitioning of  
955 oxygenated organics during the southern oxidant and aerosol study (soas) in 2013, *Aerosol Sci Tech*, 51, 30-56,  
956 10.1080/02786826.2016.1254719, 2017.  
957  
958 Tobias, H. J., and Ziemann, P. J.: Compound identification in organic aerosols using temperature-programmed thermal  
959 desorption particle beam mass spectrometry, *Anal Chem*, 71, 3428-3435, 10.1021/ac990056f, 1999.  
960  
961 Tobias, H. J., and Ziemann, P. J.: Kinetics of the gas-phase reactions of alcohols, aldehydes, carboxylic acids, and water with  
962 the c13 stabilized criegee intermediate formed from ozonolysis of 1-tetradecene, *The Journal of Physical Chemistry A*, 105,  
963 6129-6135, 10.1021/jp004631r, 2001.  
964  
965 Virtanen, A., Joutsensaari, J., Koop, T., Kannosto, J., Yli-Pirila, P., Leskinen, J., Makela, J. M., Holopainen, J. K., Poschl,  
966 U., Kulmala, M., Worsnop, D. R., and Laaksonen, A.: An amorphous solid state of biogenic secondary organic aerosol  
967 particles, *Nature*, 467, 824-827, 10.1038/nature09455, 2010.  
968  
969 Volkamer, R., Jimenez, J. L., San Martini, F., Dzepina, K., Zhang, Q., Salcedo, D., Molina, L. T., Worsnop, D. R., and  
970 Molina, M. J.: Secondary organic aerosol formation from anthropogenic air pollution: Rapid and higher than expected,  
971 *Geophys Res Lett*, 33, 10.1029/2006gl026899, 2006.  
972  
973 Williams, B. J., Goldstein, A. H., Kreisberg, N. M., and Hering, S. V.: An in-situ instrument for speciated organic  
974 composition of atmospheric aerosols: Thermal desorption aerosol gc/ms-fid (tag), *Aerosol Sci Tech*, 40, 627-638,  
975 10.1080/02786820600754631, 2006.  
976  
977 Williams, B. J., Jayne, J. T., Lambe, A. T., Hohaus, T., Kimmel, J. R., Sueper, D., Brooks, W., Williams, L. R., Trimborn,  
978 A. M., Martinez, R. E., Hayes, P. L., Jimenez, J. L., Kreisberg, N. M., Hering, S. V., Worton, D. R., Goldstein, A. H., and  
979 Worsnop, D. R.: The first combined thermal desorption aerosol gas chromatograph—aerosol mass spectrometer (tag-ams),  
980 *Aerosol Sci Tech*, 48, 358-370, 10.1080/02786826.2013.875114, 2014.  
981  
982 Williams, B. J., Zhang, Y., Zuo, X., Martinez, R. E., Walker, M. J., Kreisberg, N. M., Goldstein, A. H., Docherty, K. S., and  
983 Jimenez, J. L.: Organic and inorganic decomposition products from the thermal desorption of atmospheric particles, *Atmos.*  
984 *Meas. Tech.*, 9, 1569-1586, 10.5194/amt-9-1569-2016, 2016.  
985  
986 Yatavelli, R. L. N., Stark, H., Thompson, S. L., Kimmel, J. R., Cubison, M. J., Day, D. A., Campuzano-Jost, P., Palm, B. B.,  
987 Hodzic, A., Thornton, J. A., Jayne, J. T., Worsnop, D. R., and Jimenez, J. L.: Semicontinuous measurements of gas-particle  
988 partitioning of organic acids in a ponderosa pine forest using a movi-hrtof-cims, *Atmos Chem Phys*, 14, 1527-1546, DOI  
989 10.5194/acp-14-1527-2014, 2014.  
990  
991 Yu, J., Cocker, D. R., Griffin, R. J., Flagan, R. C., and Seinfeld, J. H.: Gas-phase ozone oxidation of monoterpenes: Gaseous  
992 and particulate products, *Journal of Atmospheric Chemistry*, 34, 207-258, 10.1023/a:1006254930583, 1999.  
993  
994 Zhang, Y. P., Williams, B. J., Goldstein, A. H., Docherty, K., Ulbrich, I. M., and Jimenez, J. L.: A technique for rapid gas  
995 chromatography analysis applied to ambient organic aerosol measurements from the thermal desorption aerosol gas  
996 chromatograph (tag), *Aerosol Sci Tech*, 48, 1166-1182, Doi 10.1080/02786826.2014.967832, 2014.  
997  
998 Zhao, Y., Kreisberg, N. M., Worton, D. R., Isaacman, G., Weber, R. J., Liu, S., Day, D. A., Russell, L. M., Markovic, M. Z.,  
999 VandenBoer, T. C., Murphy, J. G., Hering, S. V., and Goldstein, A. H.: Insights into secondary organic aerosol formation  
1000 mechanisms from measured gas/particle partitioning of specific organic tracer compounds, *Environ Sci Technol*, 47, 3781-  
1001 3787, 10.1021/es304587x, 2013a.  
1002  
1003 Zhao, Y., Kreisberg, N. M., Worton, D. R., Teng, A. P., Hering, S. V., and Goldstein, A. H.: Development of an in  
1004 sitothermal desorption gas chromatography instrument for quantifying atmospheric semi-volatile organic compounds,  
1005 *Aerosol Sci Tech*, 47, 258-266, 10.1080/02786826.2012.747673, 2013b.  
1006  
1007 Zuend, A., Marcolli, C., Booth, A. M., Lienhard, D. M., Soonsin, V., Krieger, U. K., Topping, D. O., McFiggans, G., Peter,  
1008 T., and Seinfeld, J. H.: New and extended parameterization of the thermodynamic model aiomfac: Calculation of activity

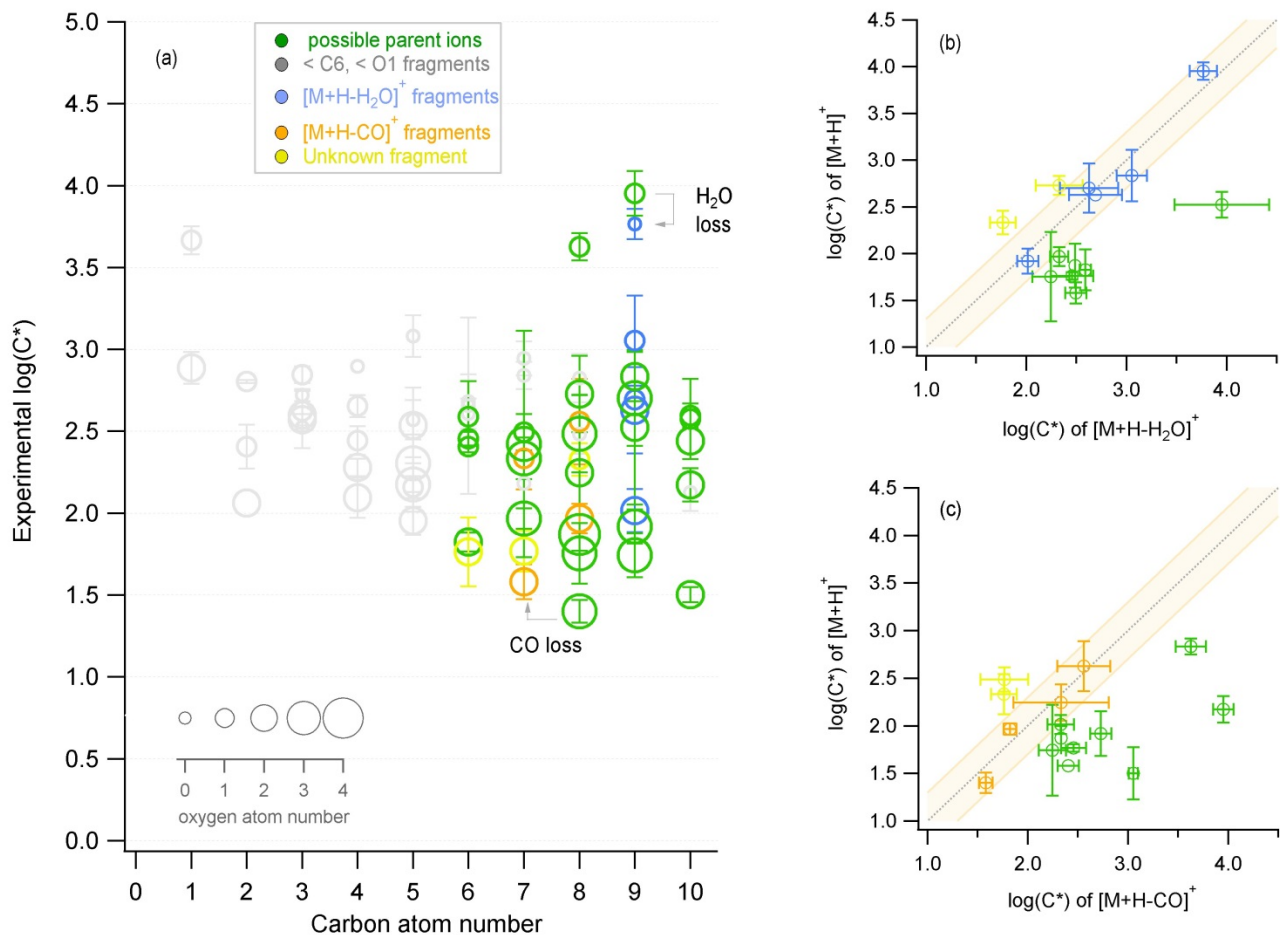
1009 coefficients for organic-inorganic mixtures containing carboxyl, hydroxyl, carbonyl, ether, ester, alkenyl, alkyl, and aromatic  
1010 functional groups, *Atmos Chem Phys*, 11, 9155-9206, DOI 10.5194/acp-11-9155-2011, 2011.  
1011  
1012  
1013

1014 Table 1: Experimental conditions during each ozonolysis experiment. Two VOC injection periods were performed for the tree  
 1015 emissions experiment.

Experiment	Ozone (ppbv)	Monoterpenes (ppbv)	Duration (h)	Maximum SOA formed ( $\mu\text{g}/\text{m}^3$ )	Chamber temperature ( $^{\circ}\text{C}$ )	SOA aging Conditions
<b><math>\beta</math>-Pinene</b>	700	120	34	130	$20 \pm 4$	Photochemical oxidation for 10 h
<b>Limonene</b>	150	25	17	50	$17 \pm 4$	Continuous $\text{NO}_3$ oxidation for 8 h
<b><math>\beta</math>-Pinene/Limonene mixture</b>	300	60/12	26	60	$19 \pm 5$	Photochemical oxidation for 4 h
<b>Tree emissions</b> 1 <sup>st</sup> inj. / 2 <sup>nd</sup> inj.	300	65/10	30	80	$30 \pm 5$	Photochemical oxidation for 6 h

1016

1017

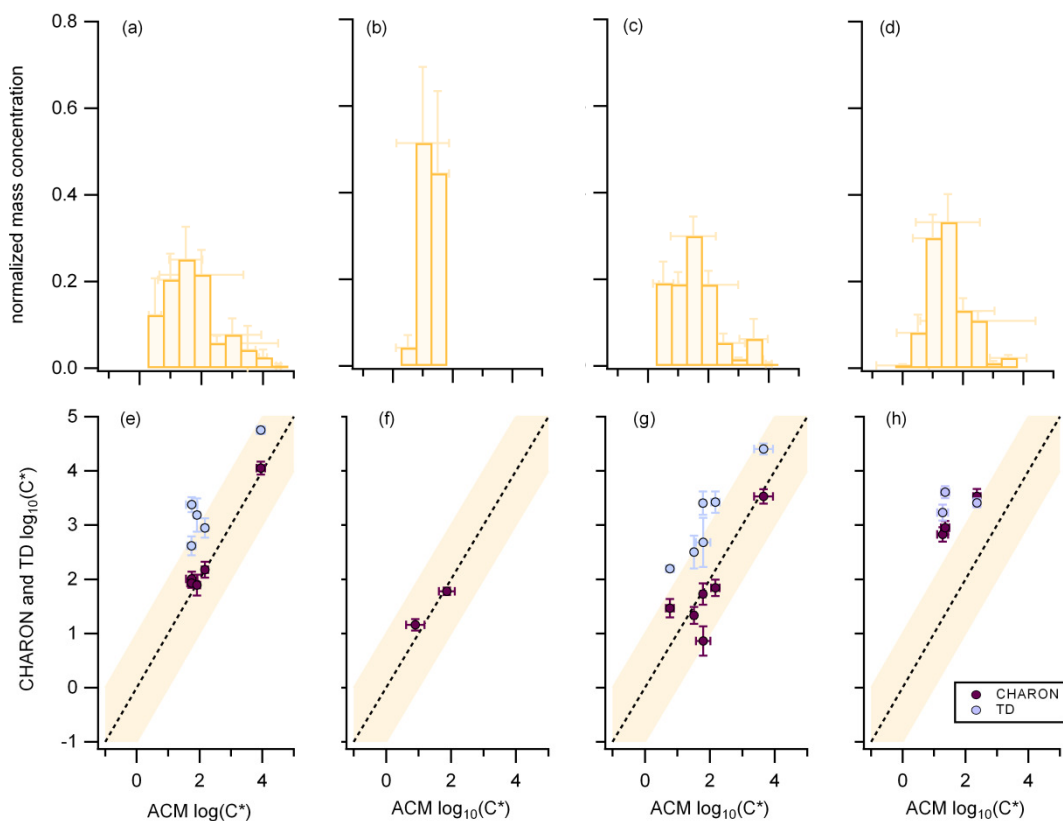


1019

1020 **Figure 1: Characteristic example of fragment identification method from the  $\beta$ -pinene ozonolysis experiment for the ACM where**  
 1021 **(a) is the experimental saturation concentration (y-axis) for all identified compounds with different carbon (x-axis) and oxygen**  
 1022 **atom number (size of markers). Different colors indicate whether the compound represents a possible parent ion (green), a**  
 1023 **fragment with carbon and oxygen atom number lower than 6 and 1 respectively (grey), or a fragment originating from the loss of**  
 1024 **water (blue) or CO (orange). This attribution results from Figure (b) and (c) which show the correlation of the saturation**  
 1025 **concentration of identified  $[M+H]^+$  ions to compounds with the same chemical formula subtracting water  $[M+H-H_2O]^+$  or CO**  
 1026  **$[M+H-CO]^+$ . If the correlation is close to the 1:1 line then the  $[M+H-H_2O]^+$  or  $[M+H-CO]^+$  compound is identified as a fragment**  
 1027 **and is given the respective color (blue or orange). If the  $[M+H-H_2O]^+$  or  $[M+H-CO]^+$  compound shows a higher volatility it is**  
 1028 **considered as a possible parent ion (green). The orange background indicates the  $\pm 0.25$  change of  $\log(C^*)$ . Error bars correspond**  
 1029 **to the error of the average ( $\pm 1\sigma$ ).**

1030

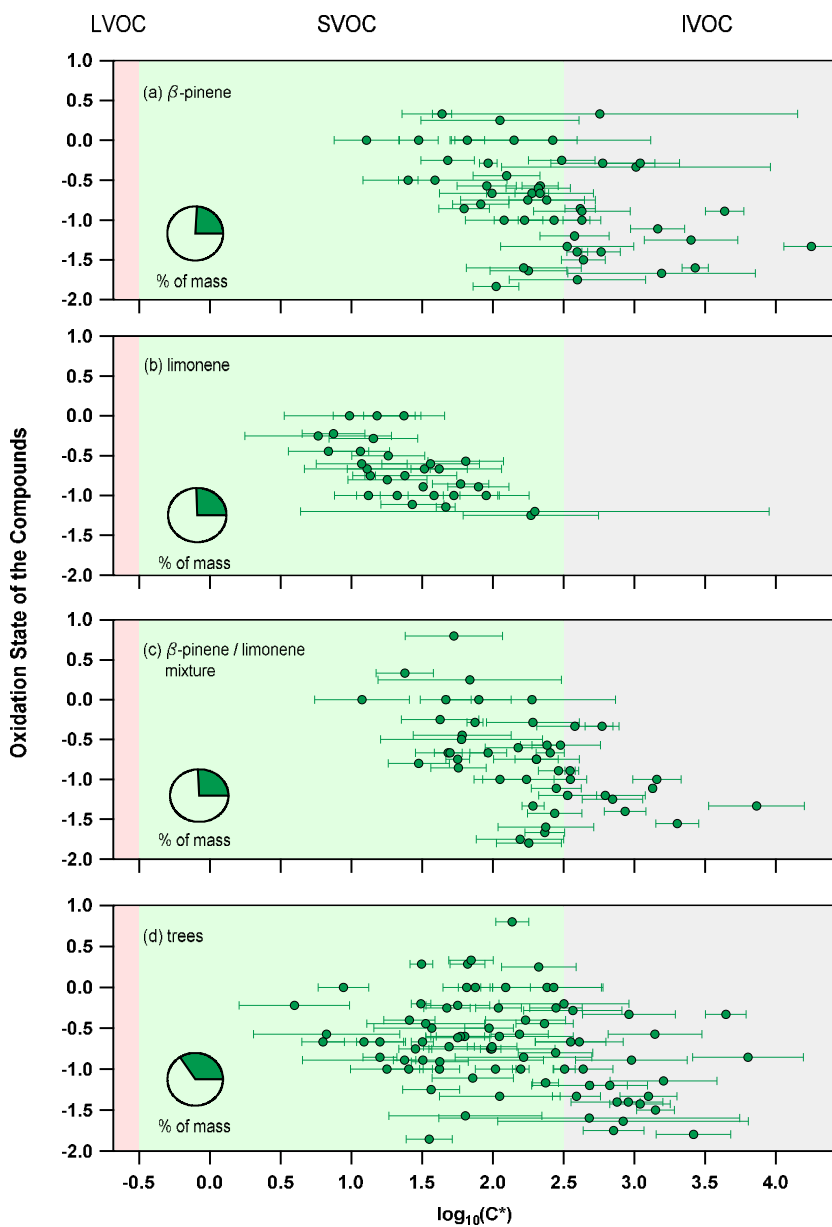




1031

1032 **Figure 2: Oxidation experiments using as precursor (a,e)  $\beta$ -pinene, (b,f) limonene, (c,g) a mixture of  $\beta$ -pinene and limonene and**  
 1033 **(d,h) real tree emissions from *Pinus sylvestris L.* (Scots pine). Upper figures (a, b, c, d) correspond to the normalized average mass**  
 1034 **concentration from ACM, CHARON and TD, distributed to the different volatility bins with a volatility resolution of  $0.5 \mu\text{g m}^{-3}$ .**  
 1035 **Bottom figures (e, f, g, h) correspond to the average volatility of overlapping compounds seen from CHARON and ACM (circles)**  
 1036 **or TD and ACM (double triangles). The dash line represents the 1:1 line. The orange background color indicates the  $\pm 1 \mu\text{g m}^{-3}$**   
 1037 **deviation from the 1:1. Error bars correspond to the  $\pm 1\sigma$  of the average throughout each experiment.**

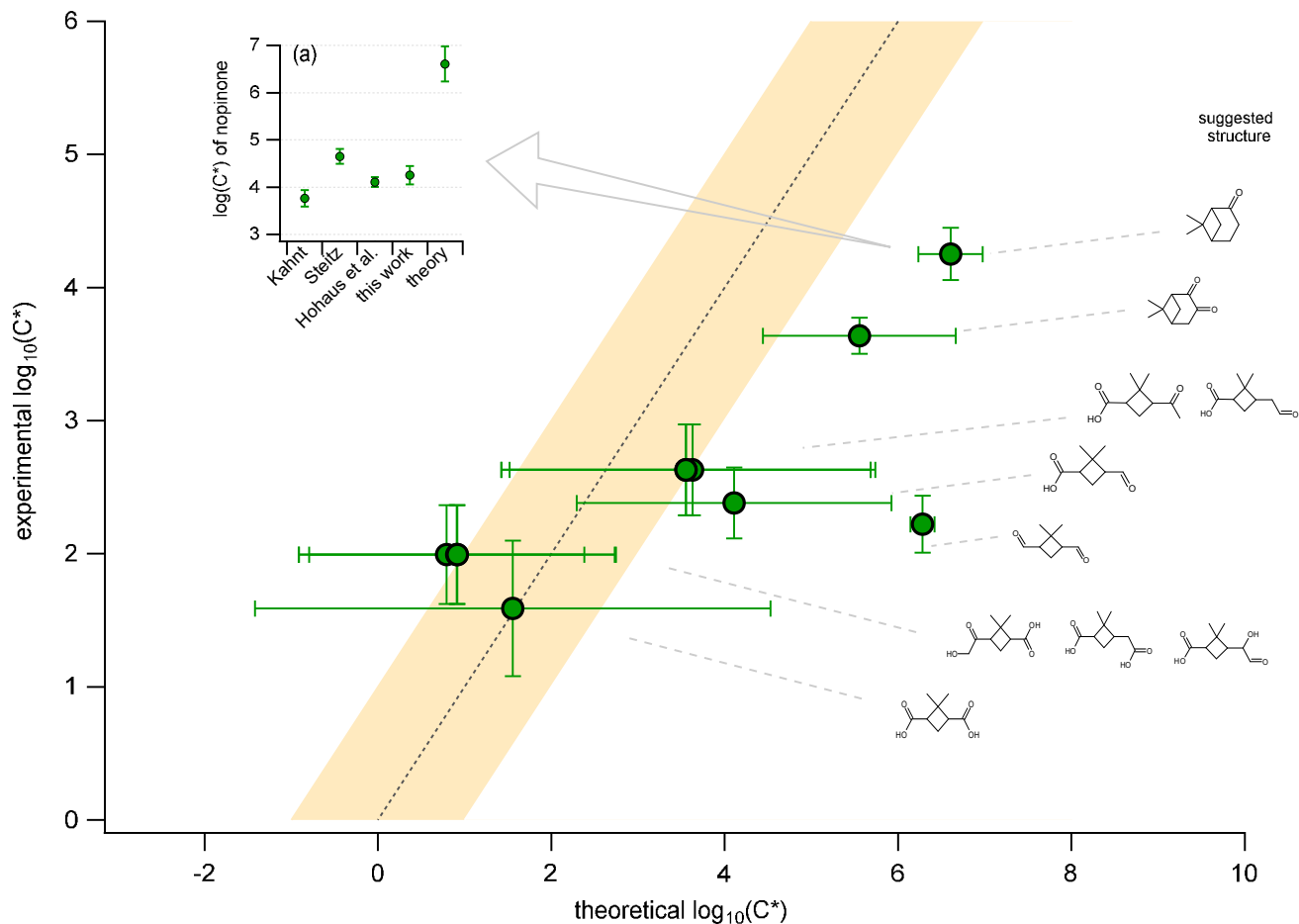
1038



1039

1040 **Figure 3: The average experimental saturation concentration for detected ions (from ACM, CHARON or TD) that act as parent**  
 1041 **ions identified using the described selection criteria during the (a)  $\beta$ -pinene, (b) limonene, (c) mixture of  $\beta$ -pinene and limonene**  
 1042 **and (d) the real tree emissions experiments. Error bars indicate the  $\pm 1\sigma$  of the experimental average. Pie charts show the percent**  
 1043 **of mass (green) measured when adding all presented ions compared to the total organic mass obtained from the AMS.**

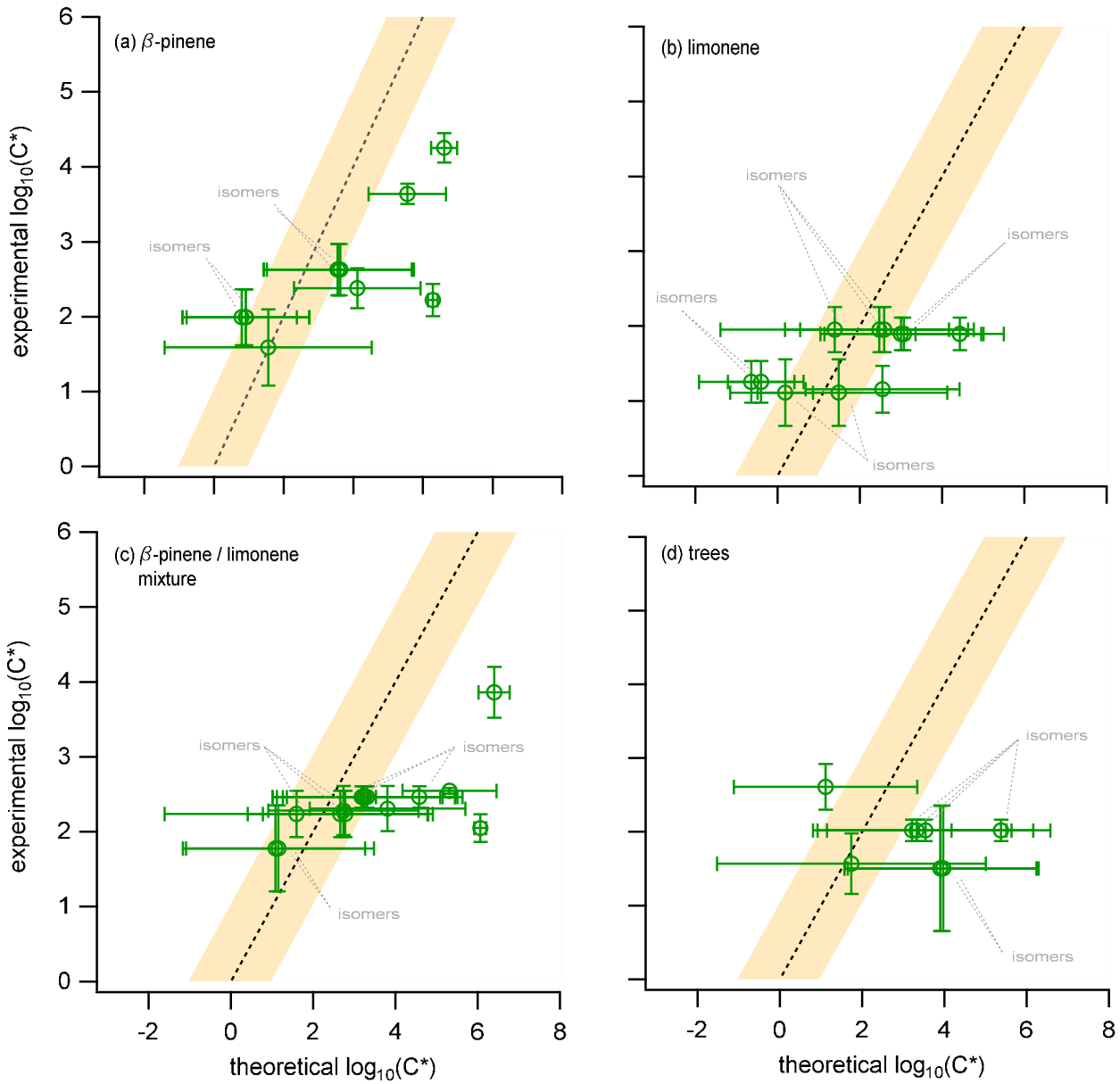
1044



1045

1046 **Figure 4: The experimental average saturation concentration obtained from all PTR-based techniques (y-axis) compared to the**  
 1047 **theoretical calculation of the saturation concentration (x-axis). Theoretical calculations were performed by assuming a chemical**  
 1048 **structure for the experimentally observed ions. The chemical structure was attributed based on known oxidation products of the**  
 1049  **$\beta$ -pinene ozonolysis experiment and are shown on the right side of the figure. Error bars on the y-axis indicate the  $\pm 1\sigma$  error of**  
 1050 **the average based on the experimental results from ACM, TD and CHARON. The error bars for the x-axis act as indicators of the**  
 1051 **minimum and maximum range of 9 different theoretical approaches with the position of the marker indicating the average of these**  
 1052 **minimum and maximum values. More details on the theoretical calculations are provided in section 2.4. Sub-figure (a) provides**  
 1053 **experimentally determined values of the saturation concentration for nopinone based on Hohaus et al. (2015) and Kahnt (2012)**  
 1054 **together with the results of the experimental and theoretical approaches from this study.**

1055



1056

1057 **Figure 5: The experimental average saturation concentration obtained from all PTR-based techniques (y-axis) compared to the**  
 1058 **theoretical calculation of the saturation concentration (x-axis) for the (i)  $\beta$ -pinene, (ii) limonene, (iii) mixture of  $\beta$ -pinene and**  
 1059 **limonene and (iv) the real tree emissions experiments. Error bars on the y-axis indicate the  $\pm 1\sigma$  error of the average based on the**  
 1060 **experimental results from ACM, TD and CHARON. The error bars for the x-axis act as indicators of the minimum and maximum**  
 1061 **range of 9 different theoretical approaches with the position of the marker indicating the average of these minimum and maximum**  
 1062 **values.**